Coupling of Wave and Circulation Models for Predicting Storm-Induced Waves, Surges, and Coastal Inundations

BY

YUNFENG CHEN, FENGYAN SHI AND JAMES T. KIRBY

RESEARCH REPORT NO. CACR-10-06
JULY 2010

CENTER FOR APPLIED COASTAL RESEARCH

Ocean Engineering Laboratory
University of Delaware
Newark, Delaware 19716

ACKNOWLEDGMENTS

This study is supported by Delaware Sea Grant Program SG0709 R/ETE-9, the Community Sediment Transport Model project of the National Oceanographic Partnership Program (NOPP) and the MORPHOS Project of the US Army Corps of Engineers, Coastal and Hydraulics Laboratory.

TABLE OF CONTENTS

LIST OF TABLES

LIST OF FIGURES

ABSTRACT

The purpose of this study is to apply coupled systems for wave-current interaction for use in simulating and predicting storm-induced surges, waves and coastal inundation. Two coupled systems are used. One includes model components: ROMS (a three-dimensional ocean model) and SWAN (a third-generation numerical wave model). The other system is NearCoM (a nearshore community model) which couples SWAN and SHORECIRC (a quasi-3D nearshore circulation model).

A coupled model system including ROMS and SWAN is based on MCT implementation. It is applied to Delaware Bay for wave and current simulation. The computational domain is a regional ocean scale domain covering the entire Delaware Bay and adjacent shelf region. Numerical results from the coupled system are compared with available wave and current data obtained from Delaware Bay Observing System (DBOS). Comparisons show good agreement between model results and observations. Strong tidal modulations of surface waves are identified in both model results and measured data.

A nearshore community model system NearCoM couples SWAN and SHORECIRC models based on the Master Program implementation. The system is used in a series of numerical experiments that are carried out in an idealized, alongshore uniform domain, which includes a planar beach, land and shelf with constant slopes, in order to explore the response of storm-induced inundation, storm surges as well as waves

to wave forcing and to different cyclone parameters through atmospheric forcing. Four sets of experiments are conducted to investigate four factors, radium of maximum wind, track of tropical cyclone, maximum wind speed as well as translation speed, respectively, in affecting storm surges and coastal inundation. Each experiment is conducted twice (with and without wave effect in the model system) to examine the wave setup effect. Coastal inundation, storm surge and wave are sensitive to all four factors. Wave setup always results in larger storm surge and inundation area.

Chapter 1

INTRODUCTION

1.1 Background

A cyclone storm is an area of closed, circular fluid motion rotating in the same direction as the Earth. Usually this is characterized by inward spiraling winds that rotate counter clockwise in the Northern Hemisphere and clockwise in the Southern Hemisphere of the Earth. Delaware Bay as a main part of the Delaware River estuary is affected and attacked by two kinds of cyclone storms: tropical cyclones (TC) as well as northeasters, from time to time and significant damage caused by those storms are recorded.

A tropical cyclone is a storm system characterized by a large low-pressure center and numerous thunderstorms that produce strong winds and heavy rain. The storm surge generated by a tropical cyclone can cause significant coastal and inland flooding which is known as one of the most serious natural disasters in the world. An average of 86 tropical cyclones of tropical storm intensity form annually worldwide (Bolonkin, 2006). It can produce not only extremely powerful winds and torrential rain, but also high waves, damaging storm surge and rip tides as well as spawning tornadoes. As recorded, storm surges can produce extensive coastal flooding up to 40 kilometers (25 mi) from the

coastline.

Northeaster can occur at any time of the year but mostly known for the presence in the winter season. It forms in the mid-latitudes and travels northward in the Atlantic Ocean with winds blowing from the northeast towards the shore along the eastern United States and Canadian coastlines. Large waves, storm surges, coastal flooding, as well as hazardous inlet currents caused by northeasters and tropical storms are a threat to people's lives, properties and navigations in Delaware's coastal regions. During the northeaster occurring on March 6-8, 1962, for example, winds reached speeds of 70 miles per hour and wind-induced waves were higher than 40 feet offshore and 20-30 feet high in the surf zone (Carey and Dalrymple, 2003). The storm surge associated with the storm was 9.5 feet at the mouth of Delaware Bay. During that event, ocean water went over highway No.1, rushed into inland bay directly and caused severe flooding disaster which resulted in damage with millions of dollars to homes, businesses, highways, and beaches in Delaware coastal communities on the ocean and inland bays. Recent statistics shows that population and development trends in coastal Delaware have placed more and more people and structures in areas subject to high winds and storm waves and tides from northeasters and, as a result, damage induced by coastal storms will probably increase. Therefore, it is necessary and important to know the physical mechanism of the response of coastal inundation to storms well in order to reduce the damage caused by storm-induced inundation to the least and to protect the Bay and the people who live there away from severe disasters and hazards.

1.2 Recent Numerical Studies on Storm Surges and Inundation

For decades, the numerical model-based storm surge forecasting systems have been developed and proved to be an important tool to reduce the loss of human lives and property damage caused by storms. In order to improve the accuracy in predicting storm surge and coastal inundation, recent model development efforts tended to include more modeling components, such as meteorology model and surface wave model, and use more complete 3D primitive hydrodynamic equations in storm surge modeling. Weisberg and Zheng (2008) compared three-dimensional and two-dimensional formulations in simulations of Ivan-like storm over Tampa Bay, Florida. They concluded that, for prediction of storm surge over complex coastal topography, a three-dimensional model may be better than two-dimensional one in modeling storm surges due to alternation of bottom stress estimates resulting from the vertical current structure. Li et al. (2006) coupled the meteorological model MM5 and the 3D regional ocean model ROMS to study hurricane-induced storm surges in Chesapeake Bay. Warner et al. (2008) incorporated the surface wave forcing into ROMS and coupled the wave model SWAN in order to predict surface waves and wave-induced circulation. Their results indicated a potential use of the coupled wave-circulation model in applications over a broader range of processes, and temporal and spatial scales.

Most numerical studies of storm surge and storm-induced coastal inundation have been site-specific. Storm surge and flooded area predicted by a numerical model in some specific domain are highly dependent on the particular site and storm. Although the geological feature may be an important factor to affect local surge and inundation,

numerical results based on a specific site may conceal the mechanism in connecting coastal inundation to atmospheric factors such as intensity, track and translation speed of a tropical cyclone. Peng et al. (2006) adopted hypothetical tropical cyclones based on parametric wind model in a rectangular domain to study tropical cyclone induced asymmetry of sea level surge and demonstrated a usefulness of such idealized numerical experiments in investigating the sensitivity of storm surge to the change of tropical cyclone parameters. In a study of storm surge and inundation in the Croatan-Albemarle-Pamlico estuary system, Peng et al. (2004) showed that, for a given storm track, the decrease of storm minimum center pressure or increase of cyclone radius of maximum wind lead to more severe storm surges and inundation. However, the predicted inundation area does not have a linear relationship with predicted surges, suggesting that the inundation area should be predicted directly by a hydrodynamic model rather than by an inland extrapolation of the predicted surge height.

Effects of wave-current interaction on storm-induced currents are believed to be of importance in predictions of storm surges and coastal inundation (Zhang and Li, 1997, Liu and Xie, 2009, and others). The wave effects can be expressed in a model in terms of radiation stresses defined by Longuet-Higgins and Stewart (1962, 1964) and recently extended to 3D applications (Mellor, 2003, 2008), wind surface stress enhanced by surface waves (Janssen, 1991), and bottom stress modified by taking into account a wave boundary layer (Styles and Glenn, 2000). In a flooded region, wave and flow patterns associated with wave-current interaction may be complex. Wave-induced setup may be significant, causing additional surges and more extensive inundation.

1.3 Outline of Present Work

In this thesis, two coupled system are applied to study the characteristics of storm-induced waves, surges and coastal inundation, as well as their response to different cyclone parameters. One the coupled system including the regional ocean circulation model ROMS and the wave generation and propagation model SWAN. The other one is the nearshore community model NearCoM which couples SWAN and the nearshore circulation model SHORECIRC. The following chapters describe the coupling framework, Delaware Bay simulation, idealized experiments and the conclusion.

Chapter 2 describes the framework of the coupled model system in detail and introduces each of the model components, ROMS, SWAN and SHORECIRC, individually, including the governing equations, numerical solution techniques, boundary conditions, and initial conditions.

Chapter 3 details the model implementation for Delaware Bay simulation. The model domain and bathymetry are presented. Grids for ROMS and SWAN are taken from Whitney (2003). Tidal forcing and wind input are specified. Currents and waves in Delaware Bay domain are simulated and results are compared with available measured current and wave data, such as current data from ADCP (Acoustic Doppler Current Profiler) and wave data from an experiment conducted in 2005 near Fourteen Ft. Bank Lighthouse in Delaware Bay.

Chapter 4 presents the model implementation for idealized experiments with focus on the response of storm-induced waves, surges and coastal inundation to wave

forcing and to different cyclone parameters in conjunction with mechanism analysis through atmospheric forcing on ocean surface. The model domain and bathymetry are explained. The bathymetry grid used for the idealized experiments are generated by software CoastGrid (Shi, 2006). Parametric wind model (Holland, 1980; Harper and Holland, 1999; Vickery et al., 2000) used in tropical cyclone wind study is explained. Sets of idealized experiments are conducted to identify the storm effect on peak storm surge, maximum significant wave height, coastal inundation as well as maximum flooding distance through following four factors, respectively: radius of maximum wind (RMW), track of the cyclone, maximum wind speed (MW) as well as the storm translation speed. Each experiment is carried out through model systems both with and without inclusion of wave effects in order to investigate the wave setup effect.

Chapter 5 summarizes the model performance. Factors in affecting storm surges, waves and coastal inundation are discussed and summarized. Conclusions are made, together with some suggestions for future work.

Chapter 2

NUMERICAL MODELS

The numerical models applied in this study are the regional ocean circulation model ROMS (Hedstrom, 2000; Shcheptkin and McWilliams, 2005), the wave generation and propagation model SWAN (Holthuijsen et al., 2004; Booij et al., 1999), and the nearshore circulation model SHORECIRC (Svendsen et al., 2000; Shi et al., 2003) implemented in the nearshore community model NearCoM (Shi et al., 2003, 2007). Two coupled model systems are used. One is coupled ROMS/SWAN system based on Model Coupling Toolkit – MCT framework for regional ocean scale applications (Warner et al., 2008). The other one is NearCoM which couples SWAN and SHORECIRC based on the Master Program (Shi et al., 2005) for nearshore scale applications. These two coupled systems are applied to simulations of waves and currents, and storm-induced coastal inundation. The details of these models are discussed here.

2.1 Coupling Framework

In the coupled ROMS/SWAN system, both ocean circulation and wave models run in a regional ocean scale domain. In the coupling processes, the ocean circulation model predicts tide- and wind-driven currents and surface elevations that are

sent to the ocean wave model in order to take into account the effects of currents and surface elevations on waves. The current effect on waves is represented by the Doppler effect in the wave dispersion relation and current effect in action balance (Holthuijsen et al., 2004). Water depth is updated using instantaneous surface elevation in the wave model, presenting the effect of surface elevation on wave predictions. The regional ocean wave model predicts wind wave generation and propagation and sends results to the ocean circulation model for calculating wave effects on currents. Surface wave forcing is based on Mellor's formulas (2008). The calculations of bottom friction associated with short wave bottom layer are based on Styles and Glenn (2000).

The coupled SWAN/SHORECIRC system is implemented in the nearshore community model NearCoM. The coupling scales are the same as in the ROMS/SWAN system. The coupled model system runs in the nearshore scale domain and predicts nearshore waves, currents, tides, surges and coastal inundation.

The coupler plays an important role in making it possible for different models to exchange information and communicate with each other at times. It is an interface of the integrated system and receives, interpolates, and sends all passing variables between different models on different computational grids.

2.2 Model Components

As mentioned above, basically there are two coupled systems developed and used in this thesis: MCT-based coupling of ocean circulation model (ROMS) and ocean wave model (SWAN), and nearshore community model (NearCoM) which itself couples

wave model （SWAN） and nearshore circulation models (SHORECIRC) based on the Master Program. Those model components are developed independently with each other and are based on different physical theories and of different model scales. Each of them can work independently as a separated numerical model. Detailed descriptions of each model component are presented as below.

2.2.1 Ocean Circulation Model - ROMS

The Regional Ocean Modeling System (ROMS; Hedstrom, 2000; Shcheptkin and McWilliams, 2005;) is a three-dimensional ocean circulation model that simulates currents, ecosystems, biogeochemical cycles and sediment movement in various coastal regions. It solves the primitive equations with the Boussinesq approximation and hydrostatic vertical momentum balance. It uses stretched, terrain-following coordinates in the vertical and orthogonal-curvilinear coordinates in the horizontal.

2.2.1.1 Equations of Motion

ROMS solves the primitive equations and below are the primitive equations in Cartessian coordinates with the equation (2.1) and equation (2.2) as momentum balance in x and y directions, respectively:

$$\frac{\partial u}{\partial t} + \vec{v}.\nabla u - fv = -\frac{\partial \phi}{\partial x} + F_u + D_u \tag{2.1}$$

$$\frac{\partial v}{\partial t} + \vec{v}.\nabla v - fu = -\frac{\partial \phi}{\partial y} + F_v + D_v \tag{2.2}$$

where all the variables are listed in Table (2.1).

Equation (2.3) and (2.4) are the advective-diffusive equations and they govern the potential temperature and salinity fields: $T(x, y, z, t)$ and $S(x, y, z, t)$.

$$\frac{\partial T}{\partial t} + \vec{v}.\nabla T = F_T + D_T \tag{2.3}$$

$$\frac{\partial S}{\partial t} + \vec{v}.\nabla S = F_S + D_S \tag{2.4}$$

Equation (2.5) is the equation of state:

$$\rho = \rho(T, S, P) \tag{2.5}$$

Equation (2.6) is the vertical momentum equation:

$$\frac{\partial \phi}{\partial z} = \frac{-\rho g}{\rho_0} \tag{2.6}$$

Equation (2.7) is the continuity equation for an incompressible fluid:

$$\frac{\partial u}{\partial x} + \frac{\partial v}{\partial y} + \frac{\partial w}{\partial z} = 0 \tag{2.7}$$

In the Boussinesq approximation, density variations are only considered in the contribution to the buoyancy force in the vertical momentum equation while they are neglected anywhere else in the momentum equations. Further assumption is made under the hydrostatic approximation that the vertical pressure gradient balances the buoyancy force. For the moment, the effects of forcing and dissipation will be represented by F and D, respectively.

2.2.1.2 Boundary Conditions

All the surface boundary conditions variables used here are list in Table (2.2). The vertical boundary conditions can be described as following two parts.

At top, equations (2.8) to (2.12) describe the boundary conditions:

$$K_m \frac{\partial u}{\partial z} = \tau_s^x(x, y, t) \tag{2.8}$$

$$K_m \frac{\partial v}{\partial z} = \tau_s^y(x, y, t) \tag{2.9}$$

$$K_T \frac{\partial T}{\partial z} = \frac{Q_T}{\rho_0 c_P} + \frac{1}{\rho_0 c_P} \frac{dQ_T}{dT}(T - T_{ref}) \tag{2.10}$$

$$K_s \frac{\partial S}{\partial z} = (E - P)S \tag{2.11}$$

$$w = \frac{\partial \zeta}{\partial t} \tag{2.12}$$

At bottom, the boundary conditions are described by equation (2.13) to equation (2.17):

$$K_m \frac{\partial u}{\partial z} = \tau_b^x(x, y, t) \tag{2.13}$$

$$K_m \frac{\partial v}{\partial z} = \tau_b^y(x, y, t) \tag{2.14}$$

$$K_T \frac{\partial T}{\partial z} = 0 \tag{2.15}$$

$$K_s \frac{\partial S}{\partial z} = 0 \tag{2.16}$$

$$-w + \vec{v}.\nabla h = 0 \tag{2.17}$$

Table 2.1: Variables used in the equations of motion

Variable	Description
D_u, D_v, D_T, D_S	Diffusive terms
F_u, F_v, F_T, F_S	Forcing terms
$f(x, y)$	Coriolis parameter
g	Acceleration of gravity
$h(x, y)$	Bottom depth
ν, κ	Horizontal viscosity and diffusivity
K_m, K_T, K_s	Vertical viscosity and diffusivity
P	Total pressure
$\phi(x, y, z, t)$	Dynamic pressure
$\rho(x, y, z, t)$	Total in situ density
$S(x, y, z, t)$	Salinity
t	Time
$T(x, y, z, t)$	Potential temperature
u, v, w	The (x, y, z) components of vector velocity
x, y	Horizontal coordinates
z	Vertical coordinate
$\zeta(x, y, t)$	The surface elevation

Table 2.2: Surface boundary condition variables

Variable	Description
$E - P$	Evaporation minus precipitation
γ_1, γ_2	Linear and quadratic bottom stress coefficients
Q_T	Surface heat flux
τ_s^x, τ_s^y	Surface wind stress
τ_b^x, τ_b^y	Bottom stress
T_{ref}	Surface reference temperature

On the variable bottom, the horizontal velocity components are constrained to accommodate a prescribed bottom stress which is a sum of linear and quadratic terms:

$$\tau_b^x = (\gamma_1 + \gamma_2 \sqrt{u^2 + v^2})u \tag{2.18}$$

$$\tau_b^y = (\gamma_1 + \gamma_2 \sqrt{u^2 + v^2})v \tag{2.19}$$

The vertical heat and salt flux may also be prescribed at the bottom; however they are usually set to zero.

As for horizontal boundary conditions, the model can be configured for a periodic channel or a doubly periodic domain. The model domain is logically rectangular, but it is possible to mask out land areas on the boundary and in the interior. Two options are provided for the boundary conditions on these masked regions: no-slip or free-slip walls.

2.2.1.3 Stretched Vertical Coordinate System

ROMS uses stretched, terrain-following coordinates (s coordinate; Song et al., 1994) in the vertical direction, which is very convenient for the computational model. It essentially flattens out the variable bottom at $z = -h(x, y)$ (Phillips, 1957; Freeman et al., 1972). Both in meteorology and oceanography have such stretched coordinate systems been used for long. The dynamic equations under such system are given in equation (2.20) to equation (2.26):

$$\frac{\partial u}{\partial t} + \vec{v}.\nabla u - fv = -\frac{\partial \phi}{\partial x} + F_u + D_u - \left(\frac{g\rho}{\rho_0}\right)\frac{\partial z}{\partial x} - g\frac{\partial \zeta}{\partial x} \tag{2.20}$$

$$\frac{\partial v}{\partial t} + \vec{v}.\nabla v - fu = -\frac{\partial \phi}{\partial y} + F_v + D_v - \left(\frac{g\rho}{\rho_0}\right)\frac{\partial z}{\partial y} - g\frac{\partial \zeta}{\partial y} \tag{2.21}$$

$$\frac{\partial T}{\partial t} + \vec{v}.\nabla T = F_T + D_T \tag{2.22}$$

$$\frac{\partial S}{\partial t} + \vec{v}.\nabla S = F_S + D_S \tag{2.23}$$

$$\rho = \rho(T, S, P) \tag{2.24}$$

$$\frac{\partial \phi}{\partial s} = \left(\frac{-gH_z\rho}{\rho_0}\right) \tag{2.25}$$

$$\frac{\partial H_z}{\partial t} + \frac{\partial (H_z u)}{\partial x} + \frac{\partial (H_z v)}{\partial y} + \frac{\partial (H_z \Omega)}{\partial s} = 0 \tag{2.26}$$

The vertical velocity in s coordinates is:

$$\Omega(x, y, s, t) = \frac{1}{H_z}\left[w - (1+s)\frac{\partial \zeta}{\partial t} - u\frac{\partial z}{\partial x} - v\frac{\partial z}{\partial y}\right] \tag{2.27}$$

and

$$w = \frac{\partial z}{\partial t} + u\frac{\partial z}{\partial x} + v\frac{\partial z}{\partial y} + \Omega H_z \tag{2.28}$$

In this system, the vertical boundary conditions also differ and at top where $s = 0$, the vertical boundary conditions are written as:

$$\left(\frac{K_m}{H_z}\right)\frac{\partial u}{\partial s} = \tau_s^x(x, y, t) \tag{2.29}$$

$$\left(\frac{K_m}{H_z}\right)\frac{\partial v}{\partial s} = \tau_s^y(x, y, t) \tag{2.30}$$

$$\left(\frac{K_T}{H_z}\right)\frac{\partial T}{\partial s} = \frac{Q_T}{\rho_0 c_p} + \frac{1}{\rho_0 c_p}\frac{dQ_T}{dT}(T - T_{ref}) \tag{2.31}$$

$$\left(\frac{K_S}{H_z}\right)\frac{\partial S}{\partial s} = (E - P)S \tag{2.32}$$

$$\Omega = 0 \tag{2.33}$$

The vertical boundary conditions for bottom at $s = -1$ are:

$$\left(\frac{K_m}{H_z}\right)\frac{\partial u}{\partial s} = \tau_b^x(x, y, t) \tag{2.34}$$

$$\left(\frac{K_m}{H_z}\right)\frac{\partial v}{\partial s} = \tau_b^y(x, y, t) \tag{2.35}$$

$$\left(\frac{K_T}{H_z}\right)\frac{\partial T}{\partial s} = 0 \tag{2.36}$$

$$\left(\frac{K_S}{H_z}\right)\frac{\partial S}{\partial s} = 0 \tag{2.37}$$

$$\Omega = 0 \tag{2.38}$$

We can see from the vertical boundary condition equations that they are simpler than those in a z-coordinate.

2.2.1.4 Horizontal curvilinear coordinates

In the horizontal directions, ROMS uses orthogonal curvilinear coordinates for the reason of solving problems with fluid in irregular regions which are the cases in a lot of realistic applications, such as flow adjacent to a coastal boundary (Hedstrom, 2000). In such situations, horizontal coordinate system is of more advantage. It is also true in many geophysical problems that the flow fields have regions of enhanced structure, which occupy a relatively small fraction of the computational domain. Then, added efficiency can be gained by placing more computational resolution in such regions. Under such conditions, the equations of motion can be re-written (Arakawa and Lamb, 1977) as follows with the new coordinate $\xi(x, y)$ and $\eta(x, y)$:

$$\frac{\partial}{\partial t}\left(\frac{H_z u}{mn}\right)+\frac{\partial}{\partial \xi}\left(\frac{H_z u^2}{n}\right)+\frac{\partial}{\partial \eta}\left(\frac{H_z uv}{m}\right)+\frac{\partial}{\partial s}\left(\frac{H_z u\Omega}{mn}\right)-\left\{\frac{f}{mn}+v\frac{\partial}{\partial \xi}\left(\frac{1}{n}\right)-u\frac{\partial}{\partial \eta}\left(\frac{1}{m}\right)\right\}H_z v$$
$$=-\left(\frac{H_z}{n}\right)\left(\frac{\partial \phi}{\partial \xi}+\frac{g\rho}{\rho_0}\frac{\partial z}{\partial \xi}+g\frac{\partial \zeta}{\partial \xi}\right)+\frac{H_z}{mn}\left(F_u+D_u\right) \quad (2.39)$$

$$\frac{\partial}{\partial t}\left(\frac{H_z v}{mn}\right)+\frac{\partial}{\partial \xi}\left(\frac{H_z uv}{n}\right)+\frac{\partial}{\partial \eta}\left(\frac{H_z v^2}{m}\right)+\frac{\partial}{\partial s}\left(\frac{H_z v\Omega}{mn}\right)-\left\{\frac{f}{mn}+v\frac{\partial}{\partial \xi}\left(\frac{1}{n}\right)-u\frac{\partial}{\partial \eta}\left(\frac{1}{m}\right)\right\}H_z u$$
$$=-\left(\frac{H_z}{n}\right)\left(\frac{\partial \phi}{\partial \eta}+\frac{g\rho}{\rho_0}\frac{\partial z}{\partial \eta}+g\frac{\partial \zeta}{\partial \eta}\right)+\frac{H_z}{mn}\left(F_u+D_u\right) \quad (2.40)$$

$$\frac{\partial}{\partial t}\left(\frac{H_z T}{mn}\right)+\frac{\partial}{\partial \xi}\left(\frac{H_z uT}{n}\right)+\frac{\partial}{\partial \eta}\left(\frac{H_z vT}{m}\right)+\frac{\partial}{\partial s}\left(\frac{H_z T\Omega}{mn}\right)=\frac{H_z}{mn}\left(F_T+D_T\right) \quad (2.41)$$

$$\frac{\partial}{\partial t}\left(\frac{H_z S}{mn}\right)+\frac{\partial}{\partial \xi}\left(\frac{H_z uS}{n}\right)+\frac{\partial}{\partial \eta}\left(\frac{H_z vS}{m}\right)+\frac{\partial}{\partial s}\left(\frac{H_z S\Omega}{mn}\right)=\frac{H_z}{mn}\left(F_s+D_s\right) \quad (2.42)$$

$$\rho=\rho(T,S,P) \quad (2.43)$$

$$\frac{\partial \phi}{\partial s}=-\left(\frac{gH_z\rho}{\rho_0}\right) \quad (2.44)$$

$$\frac{\partial}{\partial t}\left(\frac{\zeta}{mn}\right)+\frac{\partial}{\partial \xi}\left(\frac{H_z u}{n}\right)+\frac{\partial}{\partial \eta}\left(\frac{H_z v}{m}\right)+\frac{\partial}{\partial s}\left(\frac{H_z \Omega}{mn}\right)=0 \tag{2.45}$$

While the governing equations are different, all boundary conditions remain unchanged.

2.2.1.5 Numerical Solution Scheme

In the horizontal, centered and second-order finite difference approximation is used (Shcheptkin and McWilliams, 2005; Hedstrom, 2000).

In the vertical, it also uses a second-order finite-difference approximation. The model is better-behaved with a staggered horizontal grid.

ROMS is able to work with interior land areas while the computation domain actually covers the entire model domain. The land areas will be masked. And for many of the variables on those masked region, the values are set to be zero at the end of each time step.

ROMS conserves the first moments of u , v , S and T , which is accomplished by using the flux form of the momentum and tracer equations. The semi-discrete forms of the dynamic equations are then written as following equation from equation (2.46) to equation (2.51):

$$\frac{\partial}{\partial t}\left(\frac{u\overline{H_z}^{\xi}}{\overline{m}^{\xi}\overline{n}^{\xi}}\right)+\delta_{\xi}\left\{\overline{u}^{\xi}\left(\frac{\overline{uH_z}^{\xi}}{\overline{n}^{\xi}}\right)\right\}+\delta_{\eta}\left\{\overline{u}^{\eta}\left(\frac{\overline{vH_z}^{\eta}}{\overline{m}^{\eta}}\right)\right\}+\delta_{s}\left\{\overline{u}^{s}\left(\frac{\overline{\Omega H_z}}{mn}\right)\right\}$$
$$-\overline{\left\{\frac{f}{mn}+\overline{v}^{\eta}\delta_{\xi}\left(\frac{1}{n}\right)-\overline{u}^{\xi}\delta_{\eta}\left(\frac{1}{m}\right)\right\}H_z\overline{v}^{\eta}}^{\xi}=$$

$$-\frac{\overline{H_z}^{\xi}}{\overline{n}^{\xi}}\delta_\xi\phi-\frac{g\overline{H_z}^{\xi}}{\rho_0\overline{n}^{\xi}}\overline{\rho}^{\xi}\delta_\xi z-\frac{g\overline{H_z}^{\xi}}{\rho_0\overline{n}^{\xi}}(\rho_0+\overline{\rho}^{\xi})\delta_\xi\zeta+D_u+F_u \tag{2.46}$$

$$\frac{\partial}{\partial t}\left(\frac{v\overline{H_z}^{\eta}}{\overline{m}^{\eta}\overline{n}^{\eta}}\right)+\delta_\xi\left\{\overline{v}^{\xi}\left(\frac{u\overline{H_z}^{\xi}}{\overline{n}^{\xi}}\right)\right\}+\delta_\eta\left\{\overline{v}^{\eta}\left(\frac{v\overline{H_z}^{\eta}}{\overline{m}^{\eta}}\right)\right\}+\delta_s\left\{\overline{v}^{s}\left(\frac{\Omega H_z}{mn}\right)\right\}$$
$$+\left\{\frac{f}{mn}+\overline{v}^{\eta}\delta_\xi\left(\frac{1}{n}\right)-\overline{u}^{\xi}\delta_\eta\left(\frac{1}{m}\right)\right\}H_z\overline{u}^{\xi}=$$
$$-\frac{\overline{H_z}^{\eta}}{\overline{m}^{\eta}}\delta_\eta\phi-\frac{g\overline{H_z}^{\eta}}{\rho_0\overline{m}^{\eta}}\overline{\rho}^{\eta}\delta_\eta z-\frac{g\overline{H_z}^{\eta}}{\rho_0\overline{m}^{\eta}}(\rho_0+\overline{\rho}^{\eta})\delta_\eta\zeta+D_v+F_v \tag{2.47}$$

$$\frac{\partial}{\partial t}\left(\frac{hT}{mn}\right)+\delta_\xi\left(\frac{u\overline{H_z}^{\xi}\overline{T}^{\xi}}{\overline{n}^{\xi}}\right)+\delta_\eta\left(\frac{v\overline{H_z}^{\eta}\overline{T}^{\eta}}{\overline{m}^{\eta}}\right)+\delta_s\left(\overline{T}^{s}\frac{H_z\Omega}{mn}\right)=D_T+F_T \tag{2.48}$$

$$\frac{\partial}{\partial t}\left(\frac{hS}{mn}\right)+\delta_\xi\left(\frac{u\overline{H_z}^{\xi}\overline{S}^{\xi}}{\overline{n}^{\xi}}\right)+\delta_\eta\left(\frac{v\overline{H_z}^{\eta}\overline{S}^{\eta}}{\overline{m}^{\eta}}\right)+\delta_s\left(\overline{S}^{s}\frac{H_z\Omega}{mn}\right)=D_S+F_S \tag{2.49}$$

$$\rho=\rho(T,S,P) \tag{2.50}$$

$$\phi(s)=-\frac{g}{\rho_0}I_s^0 H_z\rho \tag{2.51}$$

where $\delta_\xi,\delta_\eta,\delta_s$ denote centered finite-difference approximations with the differences taken over the distances $\Delta\xi,\Delta\eta,\Delta s$ respectively. $\overline{()}^{\xi},\overline{()}^{\eta},\overline{()}^{s}$ are the averages taken over the distances $\Delta\xi,\Delta\eta,\Delta s$. I_s^0 is a second-order vertical integral computed as a sum from levels to the surface at $s=0$. The method of averaging internally conserves first moments in the model domain and it is similar to that used in Arakawa and Lamb (1997).

2.2.2 Wave Model – SWAN

Simulating WAves Nearshore (SWAN; Holthuijsen et al., 2004) is a third-generation numerical wave model. It is a spectral wave model that solves the spectral

density evolution equation (Booij et al., 1999, Ris et al., 1999). SWAN computes random, short-crested, wind-generated waves in coastal regions. It is driven by local winds and wave input through boundary conditions. The physical processes in SWAN include wave shoaling, refraction, nonlinear interaction, depth-induced breaking, wave-current interaction, bottom friction, and whitecapping dissipation. SWAN does not account for diffraction or reflection due to bottom scattering. The numerical scheme is implicit, unconditionally stable and not subject to Courant criteria. In the coupled system, it will be used for wave generation and wave propagation.

2.2.2.1 Action Balance Equation

SWAN solves for the evolution of the water spectrum by using the action density spectrum. Equation (2.52) is the governing equation for Cartesian coordinates (Hasselmann et al., 1973):

$$\frac{\partial N}{\partial t}+\frac{\partial(c_x N)}{\partial x}+\frac{\partial(c_y N)}{\partial y}+\frac{\partial(c_\sigma N)}{\partial \sigma}+\frac{\partial(c_\theta N)}{\partial \theta}=\frac{S}{\sigma} \tag{2.52}$$

where N is the action density spectrum, which is equal to the energy density spectrum divided by the relative frequency ($N(\sigma,\theta)=E(\sigma,\theta)/\sigma$). In this equation, σ and θ are wave relative frequency and wave direction, respectively. The first term in the left-hand side of equation (2.52) represents the local rate of change of wave action density spectrum in time. The second and third terms are the propagation of wave action in geographical space with velocities c_x and c_y in x and y directions, respectively. The fourth term represents shifting of the relative frequency due to variations in depths and

currents with propagation velocity c_σ in σ space. The fifth term represents depth-induced and current-induced refraction with propagation velocity c_θ in θ space. The expressions for all of propagation velocities are taken from linear wave theory (Whitham, 1974; Dingemans, 1997). The term at the right-hand side of equation (2.52) is the source term of energy density representing wind generation, energy dissipation and non-linear wave-wave interactions.

Waves obtain energy input from wind. Whitecapping, bottom friction and depth-induced wave breaking are three processes for energy dissipation in SWAN. In shallow water, bottom friction is the dominant part for dissipation while in deep water whitecapping is the main source of energy dissipation. Energy is transformed between waves by nonlinear interactions. In shallow water, triad wave-wave interactions are important while in deep water, quadruplet wave-wave interactions play a major role.

2.2.2.2 Wind Generation (S_{in})

The transfer of energy from wind to waves is modeled with a combination of resonance (Phillips, 1957) and feedback mechanisms (Miles, 1957), and the source term can be described as the sum of linear and exponential growth:

$$S_{in}(\sigma,\theta) = A(\sigma,\theta) + BE(\sigma,\theta) \tag{2.53}$$

where both A (linear growth) and BE (exponential growth) depend on wave frequency and direction as well as wind speed and direction. The expression for A can be written as equation (2.54) (Cavaleri et al., 1981) and B can be expressed as equation (2.55) (Komen et al., 1984; Janssen, 1989).

$$A = \frac{0.0015}{g^2 2\pi}\left[U_* \max(0, \cos(\theta - \theta_w)\right]^4 H \tag{2.54}$$

$$B = \max\left[0, 0.25\frac{\rho_a}{\rho_w}\left(28\frac{U_*}{c_{ph}}\cos(\theta - \theta_w) - 1\right)\right]\sigma \tag{2.55}$$

where

$$H = \exp\left(-\left(\frac{\sigma}{\sigma^*_{PM}}\right)^{-4}\right) \tag{2.56}$$

$$\sigma^*_{PM} = \frac{0.13g}{28U_*}2\pi \tag{2.57}$$

$$U_*^2 = C_D U_{10}^2 \tag{2.58}$$

in which θ_w is the wind direction, σ^*_{PM} is the peak frequency of the fully developed state according to Pierson and Moskowitz (1964), a C_D is the drag coefficient which can be expressed (WAMDI Group, 1988) as:

$$\begin{cases} C_D(U_{10}) = 1.2875\times10^{-3}, & U_{10} < 7.5m/s \\ C_D(U_{10}) = (0.8 + 0.065s/m \times U_{10})\times10^{-3}, & U_{10} \geq 7.5m/s \end{cases} \tag{2.59}$$

2.2.2.3 Dissipation (S_{ds})

The dissipation term is the summation of whitecapping $S_{ds,w}(\sigma,\theta)$, bottom friction $S_{ds,b}(\sigma,\theta)$ and depth-induced breaking $S_{ds,br}(\sigma,\theta)$.

The whitecapping formulation is given by the WAMDI group (1988) as:

$$S_{ds,w}(\sigma,\theta) = -\Gamma\tilde{\sigma}\frac{k}{\tilde{k}}E(\sigma,\theta) \tag{2.60}$$

where Γ is a coefficient that depends on steepness, k is the wave number, $\tilde{\sigma}$ is mean frequency and $\tilde{k}$ is mean wave number.

Depth-induced dissipation may be caused by bottom friction, bottom motion, percolation or back-scattering on bottom irregularities (Shemdin et al., 1978), among which bottom friction is found to be the principal mechanism (Bertotti and Cavalieri, 1994) in continental shelf seas with sandy bottoms. It can be formulated as:

$$S_{ds,b}(\sigma,\theta) = -C_{btm}\frac{\sigma^2}{g^2\sinh^2(kd)}E(\sigma,\theta) \tag{2.61}$$

where C_{btm} is friction coefficient and depends on the bottom orbital motion.

Equation (2.62) is the formulation for the total dissipation as a substitute for the process of depth-induced wave-breaking (Eldeberky and Battjes, 1995):

$$S_{ds,br}(\sigma,\theta) = \frac{D_{tot}}{E_{tot}}E(\sigma,\theta) \tag{2.62}$$

where D_{tot} is the rate of dissipation due to wave breaking and E_{tot} is the total energy (Battjes and Janssen, 1978).

2.2.2.4 Nonlinear Wave-Wave Interaction (S_{nl})

In shallow water, triad wave-wave interactions are important while in deep water, quadruplet wave-wave interactions play a major role. The formula used in SWAN is from Elderberky and Battjes (1995). As for finite-depth water, the quadruplet part can be scaled with a simple expression (Hasselmann and Hasselmann, 1981).

2.2.2.5 Boundary and Initial Conditions

The boundary conditions in SWAN in physical and spectral space are fully absorbing for wave energy that is leaving the computational domain or crossing a

coastline. The deep water boundary in coastal regions is specified by the incoming wave energy, and the lateral physical boundary in coastal regions is set to be zero, which will actually cause errors in computational areas near lateral boundaries. Therefore, it is better to set the lateral boundary sufficiently far away from the area of interest.

The shape of spectrum at the boundary of the computational grid could be defined as JONSWAP spectrum, Pierson-Moskowitz (PM) spectrum, Gaussian-shaped frequency spectrum, or simulated results provided by external model predictions.

As for initial conditions for SWAN, there are four options: computing initial spectra from the local wind velocities by using the deep water growth curve of Kahma and Calkoen (1992) and cutting off at values of significant wave height and peak frequency from Pierson and Moskowitz (1964), which is set as the default one in SWAN; setting initial spectra as $N = 0$; setting the spectra in the entire computational area by the parameters of significant wave height, peak period, peak wave direction, the coefficient of directional spreading; and reading the initial wave field from a file generated by a previous SWAN run.

2.2.2.6 Numerical Solution Scheme

SWAN uses an implicit upwind scheme (both in geographical and spectral space) because it is the most robust scheme. Hence, the discretisation of the action balance equation (2.52) is given by equation (2.63):

$$\left[\frac{N^{i_t,n}-N^{i_t,n-1}}{\Delta t}\right]_{i_x,i_y,i_\sigma,i_\theta}+\left[\frac{(c_xN)_{i_x}-(c_xN)_{i_{x-1}}}{\Delta x}\right]_{i_y,i_\sigma,i_\theta}^{i_t,n}+\left[\frac{(c_yN)_{i_y}-(c_yN)_{i_{y-1}}}{\Delta y}\right]_{i_x,i_\sigma,i_\theta}^{i_t,n}$$
$$+\left[\frac{(1-\nu)(c_\sigma N)_{i_{\sigma+1}}+2\nu(c_\sigma N)_{i_\sigma}-(1+\nu)(c_\sigma N)_{i_{\sigma-1}}}{2\Delta\sigma}\right]_{i_x,i_y,i_\theta}^{i_t,n}$$
$$+\left[\frac{(1-\eta)(c_\theta N)_{i_{\theta+1}}+2\eta(c_\theta N)_{i_\theta}-(1+\eta)(c_\theta N)_{i_{\theta-1}}}{2\Delta\theta}\right]_{i_x,i_y,i_\sigma}^{i_t,n}=\left(\frac{S}{\sigma}\right)_{i_x,i_y,i_\sigma,i_\theta}^{i_t,n^*} \quad (2.63)$$

where i_x, i_y, i_σ, i_θ are grid counters and i_t is the time level index. n^* is either n or $n-1$, which depends on the source term. ν and η are the coefficients to determine the scheme in spectral space is upwind or central (values of $\nu=0$ or $\eta=0$ indicate central schemes, which have the largest accuracy, while either of them equaling 1 correspond to upwind scheme, which is of less accurate but more robust).

In the curvilinear grid, the gradient in each grid point at location (x_i, y_i) is approximately from the upwind grid points. If the grid points are ordered in x, y space with label i, j respectively, then

$$\frac{\partial}{\partial x}c_xN=\left[\frac{[c_xN]_{i,j}-[c_xN]_{i-1,j}}{\Delta x_1-(\Delta y_1/\Delta y_2)\Delta x_2}\right]+\left[\frac{[c_xN]_{i,j}-[c_xN]_{i,j-1}}{\Delta x_2-(\Delta y_2/\Delta y_1)\Delta x_1}\right] \quad (2.64)$$

The increments are $\Delta x_1 = x_{i,j}-x_{i-1,j}$, $\Delta x_2 = x_{i,j}-x_{i,j-1}$, $\Delta y_1 = y_{i,j}-y_{i-1,j}$ and $\Delta y_2 = y_{i,j}-y_{i,j-1}$. The other terms in Equation (2.63) are discretized in the same way.

2.2.3 Nearshore Circulation Model - SHORECIRC

SHORECIRC (Svendsen et al., 2000) is a quasi-3D nearshore circulation

model for prediction of wave-induced nearshore circulation in the nearshore ocean, between the shoreline and about 10 m water depth. It is a 2D horizontal model which incorporates the effect of the vertical structure of horizontal flows. The curvilinear version of SHORECIRC (Shi et al, 2003, 2007) is applied in this study using a stretched coordinate.

2.2.3.1 Governing Equations

With the coordinate transformations given by equation (2.65):

$$\begin{cases} \xi_1 = \xi_1(x_1, x_2) \\ \xi_2 = \xi_2(x_1, x_2) \\ z = z \end{cases} \tag{2.65}$$

where (x_1, x_2, z) are spatial independent variables in rectangular Cartesian coordinates and (ξ_1, ξ_2, z) are new independent variables in the transformed image domain, the depth-integrated, short-wave-averaged continuity equation and momentum equation in terms of contravariant components are given by (Shi et al., 2003):

$$\frac{\partial \bar{\zeta}}{\partial t} + \frac{1}{\sqrt{g_0}} \frac{\partial}{\partial \xi_\partial} \left(\sqrt{g_0} \overline{V}^\partial h \right) = 0 \tag{2.66}$$

$$\begin{aligned} &\frac{\partial}{\partial t}\left(\tilde{V}^\alpha h\right) + \frac{1}{\sqrt{g_0}} \frac{\partial}{\partial \xi_\beta} \left[\sqrt{g_0} \left(\tilde{V}^\alpha \tilde{V}^\beta h + A_{\alpha\beta\delta} \tilde{V}^\delta \right) \right] + \left(\tilde{V}^\gamma \tilde{V}^\beta h + A_{\gamma\beta\delta} \tilde{V}^\delta \right) \Gamma^\alpha_{\gamma\beta} \\ &+ \frac{1}{\rho\sqrt{g_0}} \frac{\partial}{\partial \xi_\beta} \left[\sqrt{g_0} \left(S^{\alpha\beta} + \rho M_{\alpha\beta} \right) \right] + \frac{1}{\rho} \left(S^{\gamma\beta} + \rho M_{\gamma\beta} \right) \Gamma^\alpha_{\gamma\beta} \\ &+ ghg^{\beta\alpha} \frac{\partial \bar{\zeta}}{\partial \xi_\beta} + \frac{\tau_B^\alpha}{\rho} + \frac{1}{\sqrt{g_0}} \frac{\partial}{\partial \xi_\beta} \left\{ \sqrt{g_0} \left[T^{\alpha\beta} - h\left(D_{\delta\beta} \tilde{V}^\alpha_{,\delta} + D_{\delta\alpha} \tilde{V}^\beta_{,\delta} \right) \right] \right\} \\ &+ \left[T^{\alpha\beta} - h\left(D_{\delta\beta} \tilde{V}^\gamma_{,\delta} + D_{\delta\gamma} \tilde{V}^\beta_{,\delta} \right) \right] \Gamma^\alpha_{\gamma\beta} - \frac{1}{\sqrt{g_0}} \frac{\partial}{\partial \xi_\beta} \left[\sqrt{g_0} \left(hB_{\alpha\beta} \tilde{V}^\delta_{,\delta} \right) \right] - \left(hB_{\gamma\beta} \tilde{V}^\delta_{,\delta} \right) \Gamma^\alpha_{\gamma\beta} = 0 \end{aligned} \tag{2.67}$$

where: $\tilde{V}^{\alpha}$ is the component of depth-averaged and short-wave averaged velocity; g_0 is the determinant of the metric tensor $g_{\alpha\beta}$,

$$g_0 = \begin{vmatrix} g_{11} & g_{12} \\ g_{21} & g_{22} \end{vmatrix} \tag{2.68}$$

in which,

$$g_{\alpha\beta} = \frac{\partial x_\gamma}{\partial \xi_\alpha}\frac{\partial x_\gamma}{\partial \xi_\beta} \tag{2.69}$$

and $\Gamma^{\alpha}_{\gamma\beta}$ is the Christoffel symbol of the second kind. τ_S^{α} and τ_B^{α} are the contraviant components of the surface shear stress and the bottom shear stress, respectively. $S^{\alpha\beta}$ and $T^{\alpha\beta}$ are the contravariant components of the short-wave-induced radiation stress tensor and the depth-integrated Reynolds' stress tensor, respectively. The relationship between $S^{\alpha\beta}$ and $S_{\alpha\beta}$ is as following:

$$S^{11} = \frac{1}{g_0}\left(S_{11}\left(\frac{\partial x_2}{\partial \xi_2}\right)^2 - 2S_{12}\frac{\partial x_2}{\partial \xi_2}\frac{\partial x_1}{\partial \xi_2} + S_{22}\left(\frac{\partial x_1}{\partial \xi_2}\right)^2 \right) \tag{2.70}$$

$$S^{12} = S^{21} = \frac{1}{g_0}\left(-S_{11}\left(\frac{\partial x_2}{\partial \xi_1}\frac{\partial x_2}{\partial \xi_2}\right) + S_{12}\left(\frac{\partial x_1}{\partial \xi_1}\frac{\partial x_2}{\partial \xi_2} + \frac{\partial x_2}{\partial \xi_1}\frac{\partial x_1}{\partial \xi_2}\right) - S_{22}\left(\frac{\partial x_1}{\partial \xi_1}\frac{\partial x_1}{\partial \xi_2}\right)\right) \tag{2.71}$$

$$S^{22} = \frac{1}{g_0}\left(S_{11}\left(\frac{\partial x_2}{\partial \xi_1}\right)^2 - 2S_{12}\frac{\partial x_1}{\partial \xi_1}\frac{\partial x_2}{\partial \xi_1} + S_{22}\left(\frac{\partial x_1}{\partial \xi_1}\right)^2 \right) \tag{2.72}$$

2.2.3.2. Boundary Conditions

Boundary conditions implemented in the curvilinear SHORECIRC model include wall boundary condition, specified-flux boundary condition, specified surface elevation boundary condition, periodic boundary condition, and moving shoreline boundary condition.

Slip boundary conditions can be used for lateral walls, shoreline and boundaries of structures inside a computational domain. The contravariant technique can simplify the expressions of slip boundary conditions in curvilinear coordinates. For a curvilinear boundary, the slip boundary condition can be simply expressed as:

$$\tilde{V}^{\alpha} = 0 \tag{2.73}$$

As for flux boundary, a specific boundary condition is implemented by using the contravariant component. The contravariant component of the specified velocity (or flux) can be obtained using the transformation relation:

$$v^{\alpha} = \frac{\partial \xi_{\alpha}}{\partial x_{\beta}} v_{\beta} \tag{2.74}$$

where v^{α} and v_{β} are contravariant components and Cartesian components, respectively.

Specified surface elevation boundary conditions are usually used for given tidal elevations at SHORECIRC boundaries or for model nesting between different scale circulation models.

A periodic boundary condition along cross-shore boundaries at the two ends of the domain is also an option in this model for simulations of uniform beaches. It means that the instantaneous flow at each point of one of the cross-shore boundaries is mirrored at the equivalent point of the other cross-shore boundary. The periodic boundary condition requires both the bathymetry and the grid to be periodic.

A moving boundary condition is implemented using a combined wet-dry method. The velocity at the moving boundary is obtained by a modified Riemann solver and the shoreline is defined as an interface between dry and wet fixed grid points. The

moving boundary algorithm is used in the whole computation domain including shoreline boundaries and inner structure boundaries.

2.2.3.3. Wind Surface Stress

The wind-induced surface stress is computed as (Church and Thornton, 1993; Smith et al., 1993):

$$\tau_\alpha^S = C_D \rho_\alpha |W| W_\alpha \tag{2.75}$$

where, ρ_α is the air density and W is the wind velocity at 10 m elevation. And C_D is the drag coefficient, which again is computed from the formula recommended by the WAMDI group (1988) as in equation (2.59).

2.2.3.4. Numerical Solution Scheme

The curvilinear SHORECIRC provides two options based on, respectively, high-order explicit numerical schemes, and the second-order semi-implicit schemes.

A staggered grid is used in the model. Various points types are defined in the model code to recognize different boundary conditions, which allows the model to be used in complicated domains such as harbors and tidal inlets. The point-type specification can be done by either using the grid generation program CoastGrid (http://coastal.udel.edu/~fyshi/coastgrid/coastgrid.html) or specifying negative water depths at land points.

In the high-order explicit scheme, the first-order spatial derivative terms are discretized to fourth-order accuracy using five-point finite-differencing. For example, f_{ξ_1}

may be discretized at point j as:

$$f_{\xi_1} = \left(f_{j-2} - 27f_{j-1} + 27f_j - f_{j+1}\right)/\left(24\Delta\xi_1\right) + o\left(\delta\xi_1^4\right) \tag{2.76}$$

The fourth-order Adams-Bashforth-Moulton predictor-corrector scheme is employed to perform time updating. A sequence of time instants are defined by $t = p\Delta t$. Level p refers to information at the present, known time level. For the time-derivative equation written by

$$\frac{\partial f}{\partial t} = E \tag{2.77}$$

the predictor step is the third-order explicit Adams-Bashforth scheme, given by:

$$f_{i,j}^{p+1} = f_{i,j}^{p} + \frac{\Delta t}{12}\left[23\left(E\right)_{i,j}^{p} - 16\left(E\right)_{i,j}^{p-1} + 5\left(E\right)_{i,j}^{p-2}\right] \tag{2.78}$$

After predictor step we use the fourth-order Adams-Moulton corrector method：

$$f_{i,j}^{p+1} = f_{i,j}^{p} + \frac{\Delta t}{12}\left[9\left(E\right)_{i,j}^{p+1} + 19\left(E\right)_{i,j}^{p} - 5\left(E\right)_{i,j}^{p-1} + 3\left(E\right)_{i,j}^{p-2}\right] \tag{2.79}$$

As an alternative option, the second-order semi-implicit numerical schemes can be used for long-term simulations. The second-order semi-implicit numerical schemes are developed based on a splitting method in which the gravity wave mode and vorticity wave mode are solved separately. The gravity mode is basically presented in the form of the ordinary nonlinear shallow water equations as:

$$\frac{\delta}{\delta t}\left(\tilde{V}^{\alpha}h\right) + \frac{1}{\sqrt{g_0}}\frac{\partial}{\partial\xi_\beta}\left[\sqrt{g_0}\left(\tilde{V}^{\alpha}\tilde{V}^{\beta}h\right)\right] + \tilde{V}^{\gamma}\tilde{V}^{\beta}h\Gamma_{\gamma\beta}^{\alpha} + ghg^{\beta\alpha}\frac{\partial\bar{\varsigma}}{\partial\xi_\beta} + \frac{\tau_B^{\alpha}}{\rho} = 0 \tag{2.80}$$

The vorticity mode includes the lateral mixing and the 3D dispersion effects. Radiation stresses are also calculated in the vorticity mode:

$$\frac{\delta}{\delta t}\left(\tilde{V}^{\alpha}h\right)+\frac{1}{\sqrt{g_0}}\frac{\partial}{\partial\xi_\beta}\left[\sqrt{g_0}\left(A_{\alpha\beta\delta}\tilde{V}^{\delta}\right)\right]+A_{\gamma\beta\delta}\tilde{V}^{\delta}\Gamma^{\alpha}_{\gamma\beta}$$
$$+\frac{1}{\rho\sqrt{g_0}}\frac{\partial}{\partial\xi_\beta}\left[\sqrt{g_0}\left(S^{\alpha\beta}+\rho M_{\alpha\beta}\right)\right]+\frac{1}{\rho}\left(S^{\gamma\beta}+\rho M_{\gamma\beta}\right)\Gamma^{\alpha}_{\gamma\beta}$$
$$+\frac{1}{\sqrt{g_0}}\frac{\partial}{\partial\xi_\beta}\left\{\sqrt{g_0}\left[T^{\alpha\beta}-h\left(D_{\delta\beta}\tilde{V}^{\alpha}_{,\delta}+D_{\delta\alpha}\tilde{V}^{\beta}_{,\delta}\right)\right]\right\}$$
$$+\left[T^{\gamma\beta}-h\left(D_{\delta\beta}\tilde{V}^{\gamma}_{,\delta}+D_{\delta\gamma}\tilde{V}^{\beta}_{,\delta}\right)\right]\Gamma^{\alpha}_{\gamma\beta}$$
$$-\frac{1}{\sqrt{g_0}}\frac{\partial}{\partial\xi_\beta}\left[\sqrt{g_0}\left(hB_{\alpha\beta}\tilde{V}^{\delta}_{,\delta}\right)\right]-\left(hB_{\gamma\beta}\tilde{V}^{\delta}_{,\delta}\right)\Gamma^{\alpha}_{\gamma\beta}=0 \tag{2.81}$$

The gravity mode will be solved semi-implicitly using the regular alternative-direction-implicit method which is verified to be a CFL-free method for linearized equations (Casulli and Zanolli, 2002). Substituting the discretized equation (2.80) into equation (2.81) leads to the surface elevation alone euqation：

$$-\frac{Ea(i)}{J\Delta\xi_1^2R}\bar{\varsigma}_{i-1}+\bar{\varsigma}_i-\frac{Ea(i+1)}{J\Delta\xi_1^2R}\bar{\varsigma}_{i+1}=\frac{1}{R}\left(\frac{Eb(i+1)-Eb(i)}{J\Delta\xi_1}-\frac{\partial\tilde{v}}{J\partial\xi_2}+\frac{2}{\Delta t}\bar{\varsigma}_i^{-dt}\right) \tag{2.82}$$

where Ea, Eb and R are coefficients from the derivation. Equation (2.82) can be solved fully implicitly and $\tilde{V}^{\alpha}$ can be calculated directly form the following formulation:

$$\tilde{V}^{\alpha}=-Ea\frac{\partial\bar{\varsigma}}{\partial\xi_\alpha}+Eb \tag{2.83}$$

The vorticity mode is solved using explicit schemes.

2.2.4 Couplers

Warner et al. (2008) described a coupled system based on ROMS and SWAN using the Model Coupling Toolkit (MCT; Larson, et al., 2004; Jacob et al., 2005) framework. The MCT allows the transmission and transformation of various distributed

data between component models comprising a parallel coupled system. MCT is a public domain program and is complied as a set of libraries. Those libraries are linked during the compilation. The coupler used in NearCoM to couple SWAN and SHORECIRC is based on the Master Program (Shi, et al., 2005; Shi, et al., 2009).

Chapter 3

DELAWARE BAY SIMULATION

In this chapter, the coupled ROMS/SWAN system is used to simulate locally generated wave conditions in Delaware Bay simulation. First, the model setup for Delaware Bay will be specified, such as the model domain and the model grids. Then the calibrated system is applied to Delaware Bay for validation. Two experiments will be presented. One is a tidal elevation simulation in Delaware Bay. The numerical results of M2 tidal harmony constituents at five sea level stations are compared with observation data obtained online from National Oceanic and Atmospheric Administration (NOAA) website. Also, the coupled system is used to run simulation of waves and currents in the Bay from May 22 to May 29, 2005 and the numerical results are compared with an observation data set from a Wave Sentry Buoy (WSB; Qin, 2005).

3.1 Model Setup

The coupled ROMS/SWAN system is applied into Delaware Bay for simulation and prediction of currents and waves along Delaware's coast. Delaware Bay is a semi-enclosed bay, and the waves in the bay are mostly locally generated wind waves. Ocean swell from the Atlantic Ocean only affects the region near the mouth of the bay.

3.1.1 Model Domain

ROMS and SWAN are run in a regional ocean scale domain which covers the entire Delaware Bay as well as the adjacent shelf region (Figure 3.1) with the corresponding bathymetry (Figure 3.2, Whitney, 2003). The offshore boundary is along the 100m isobath. An orthogonal curvilinear grid is generated using the Gridpack grid generation software (Wilkin and Hedstrom, 1991) as shown in Figure 3.3. The grids contains 150 × 300 cells and covers an area of 240 km × 340 km. The highest horizontal resolution is around 0.75 km in the bay while the lowest resolution is 8 km offshore, which reduces grid number efficiently in calculation. Figure 3.4 shows the grid cell size where left panel shows the grid cell size in longitude direction and right panel shows the grid cell size in latitude direction.

3.1.2 Tidal Forcing in ROMS

ROMS is able to propagate the different tidal constituents from its lateral boundaries. In the simulation, ROMS is driven by the M2, S2, N2, K2, K1, O1, P1 and Q1 tides at the offshore boundary in the model domain of Delaware Bay and its adjacent ocean region. Tidal data are derived from the Oregon State University global models of ocean tides TPX06 and TPX07 (Egbert and Erofeeva, 2002). The tidal forcing files are created using ROMSTOOLS (Penven and Tan, 2007).

3.1.3 Wind Data for SWAN

The wind speed and direction data derived from DBOS are used to construct the wind field for SWAN. The data are measured near the Fourteen Ft. Bank Lighthouse and 18 m above the mean sea surface, while the wind speed specified at the standard elevation of 10 m above the mean sea surface is needed in SWAN. Therefore, the data are adjusted by $U_{10}/U_z = (10/z)^{1/7}$ (Johnson, 1999), where U_{10} is the wind speed 10 m above the mean sea surface, z is the elevation where the wind speed is measured, and U_z is the wind speed at the elevation of z meter.

3.2 Ocean Circulation Model Validation

ROMS was validated using the single M2 tidal constituent, the major tidal component in Delaware Bay. Tidal harmonics for M2 derived from TPX06 are applied at open boundaries as the model input. Figure 3.5 shows M2 tidal magnitude distribution in the computational domain with tidal elevation amplitude on the left panel and tidal elevation phase on the right panel. A reasonably good agreement with the data is found at several measurement stations in Delaware Bay. Data are obtained online from NOAA website (http://tidesandcurrents.noaa.gov). Five sea level stations within Delaware Bay domain are chosen for the comparison between numerical results and observations: Atlantic City (Latitude: $39^o21.3^{'}N$; Longitude: $74^o25.1^{'}W$), Cape May (Latitude: $38^o58.1^{'}N$; Longitude: $74^o57.6^{'}W$), Lewes (Latitude: $38^o46.9^{'}N$; Longitude: $74^o7.2^{'}W$), Delaware City (Latitude: $39^o34.9^{'}N$; Longitude: $75^o35.3^{'}W$) and Brandywine Shoal Light (Latitude: $38^o59.2^{'}N$; Longitude: $75^o6.8^{'}W$). Detailed

comparison is listed in Table 3.1. All comparisons in this table show good agreement between numerical model results and the observations except the phase comparison at Delaware City. It is mainly because Delaware City station is located in the Chesapeake and Delaware Canal, which is not included in the model. But generally, the results showed in Table 3.1 indicate a fairly good performance of the model.

Table 3.1: Comparison of M2 harmonic constituents between model result and NOAA data

Sea Level Station	M2 Amplitude (m)		M2 Phase (degree)	
	NOAA Data	Model Result	NOAA Data	Model Result
Atlantic City	0.594	0.5774	355.4	359.83
Cape May	0.714	0.7088	28.6	27.7642
Lewes	0.616	0.6315	31.1	30.3668
Delaware City	0.744	0.7496	29.0	89.4406
Brandywine Shoal Light	0.722	0.7083	36.9	34.703

3.3 Current and Wave Simulation

We applied the coupled ROMS/SWAN system to wave and current simulations in Delaware Bay from May 01, 2005 to May 30, 2005. The bottom friction is

calculated using the Madsen (1988) formulation with $K_n = 0.05m$. Qin (2005) did similar experiments using the I/O scheme exchanging wave and current information between models, while in this study, we use the coupled s ROMS/SWAN system.

In 2005, a Wave Sentry Buoy (WSB) was deployed during May 22 through May 27, 2005 near Fourteen Ft. Bank Lighthouse at around $39^o01^{'}N$ and $75^o11^{'}W$. The raw data are processed to provide directional and non-directional spectra. The significant wave height and non-directional frequency spectrum are compared between SWAN results and WSB's.

The wind information measured at the lighthouse in the period of 00:00 May 22 through 23:00 May 29 is available. Since difference of simulation in Delaware Bay between a spatial uniform wind field and a spatial varying wind field is small (Qin, 2005), only wind speed and direction from the lighthouse are used to construct the wind field for SWAN. Figure 3.6 records the wind speed (upper panel) and direction (lower panel) at Fourteen Ft. Bank Lighthouse during 00:00 May 24 through 18:00 May 26, 2005.

ROMS is run with 8 tidal constituents M2, S2, N2, K2, K1, O1, P1 and Q1 tides at the offshore boundary and those tidal constituents are, again, derived from TPX06.

The comparison of depth-averaged current velocity between measurement of ADCP (dot) and model simulation (solid line) at Fourteen Ft. Bank Lighthouse in May, 2005 are presented in Figure 3.7 (East-West depth-averaged current velocity) and Figure 3.8 (North-South depth-averaged current velocity).

Some statistical parameters are calculated for data analysis, such as Mean

Error (ME), Mean Absolute Error (MAE), Root Mean Square Error (RMSE), and Index of agreement or relative error (IOA), which reflect the degree that observations agree with model results (Padilla-Hernandez et al., 2004). The definitions are given by:

$$ME = \frac{1}{N}\sum_{i=1}^{N}(M_i - O_i) \tag{3.1}$$

in which, O_i is the observation data while M_i is the model results

$$MAE = \frac{1}{N}\sum_{i=1}^{N}\left|M_i - O_i\right| \tag{3.2}$$

$$RMSE = \sqrt{\frac{1}{N}\sum_{i=1}^{N}(M_i - O_i)^2} \tag{3.3}$$

$$IOA = 1 - \frac{\sum_{i=1}^{N}(M_i - O_i)^2}{\sum_{i=1}^{N}\left[\left|M_i - \overline{M}\right| + \left|O_i - \overline{O}\right|\right]^2} \tag{3.4}$$

in which, $\overline{M} = \sum_{i=1}^{N} M_i$ and $\overline{O} = \sum_{i=1}^{N} O_i$.

Using these statistical parameters as the criteria for the model validation lends to a more reasonable way to compare the model simulation results with the observations. Table 3.2 presents the statistical parameters for East-West depth-averaged current velocity and North-South depth-averaged current velocity. From the table, we can see clearly that both simulations of E-W depth-averaged current velocity and N-S depth-averaged current velocity have a very good agreement with observations. Both of the IOA-s are greater than 0.9, which indicates good performance of the coupled model system in Delaware Bay simulation.

Figure 3.9 is the comparison of significant wave height at Fourteen Ft. Bank Lighthouse during May 24 through May 27, 2005 between measured data at WSB (solid

line) and numerical result (dash line). During most of the time periods, the model overestimates the significant wave height while in some periods, such as period from 8:00, May 26 to 16:00, May 26, it underestimates the significant wave height. But overall, the figure shows a good agreement between model and measurement.

Table 3.2: Statistical comparison for depth-averaged current velocity (m/s) between model result and ADCP measurement at Fourteen Ft. Bank Lighthouse in May, 2005

	East-West depth-averaged current velocity	North-South depth-averaged current velocity
ME	0.0286	-0.050834
MAE	0.0597	0.1585
RMSE	0.074427	0.18937
IOA	0.91801	0.95689

Data-model comparison of wave energy is presented in Figure 3.10. The wave energy for model is computed by the sum of the spectrum get directly from model output. As for observation, the wave energy is computed by formula of $Energy = (Hs/4)^2$, where H_s is WSB measurement. The comparison between wave energy shows a good agreement between model and observation.

As for peak frequency, the model produces reasonably good result during time period from 18:00 May 24 to 8:00 May 26, compared to the WSB measurement. However, during other time periods, the simulated peak frequency is overestimated compared to observation, which is shown in Figure 3.11.

Again, some basic statistical parameters are computed for the quantitative analysis, and the results are shown in Table 3.3. It shows clearly that the coupled model system gives very good performance on simulation of significant wave height and wave energy while the simulation of peak frequency does not fit the observation very well.

Table 3.3: Statistical comparison for significant wave height, wave energy and peak frequency between model result and WSB measurement at Fourteen Ft. Bank Lighthouse

	Significant wave height (m)	Wave energy (m^2)	Peak frequency (Hz)
ME	0.0281	0.0015815	0.06539
MAE	0.072761	0.0049228	0.072109
RMSE	0.094387	0.0069142	0.11861
IOA	0.95183	0.93578	0.1728

Figure 3.12 shows the comparison of spectrum between model and measured data from WSB at Fourteen Ft. Bank Lighthouse. The model result (right panel) correctly

simulated time stack of frequency spectrum compared to experiment data (middle panel) but with overestimated value of peak frequency spectrum. Both the experiment data and the model result show strong tidal modulations of surface waves, indicating the importance of wave-current interaction in the physical process.

3.4 Summary

Current results from ROMS as well as wave results from SWAN are compared with available observations. Tidal harmonic analysis is conducted to get the M2 tidal harmonic constituent which is in a good agreement with data derived from NOAA website at five sea level stations. The simulated current velocities at the measuring station are compared with data from ADCP. Statistical analysis of model results and observation indicates that both the N-S depth-averaged velocity and E-W depth-averaged velocity fit the ADCP data well with high IOA of 0.95689 and 0.91801, respectively. Significant wave height, wave energy as well as peak frequency of Fourteen Ft. Bank Lighthouse simulated by the coupled model system are compared with WSB data. Statistical analysis shows that simulations of significant wave height and wave energy fit the data very well. Predicted peak frequency fits the data well during 18:00 May 24 to 8:00 May 26 but overestimates the value during other time periods. The model correctly simulated time stack of frequency spectrum compared to experiment data and both numerical result and measured data show strong tidal modulations of surface waves, which indicate the importance of taking into consideration of wave-current interaction during numerical modeling.

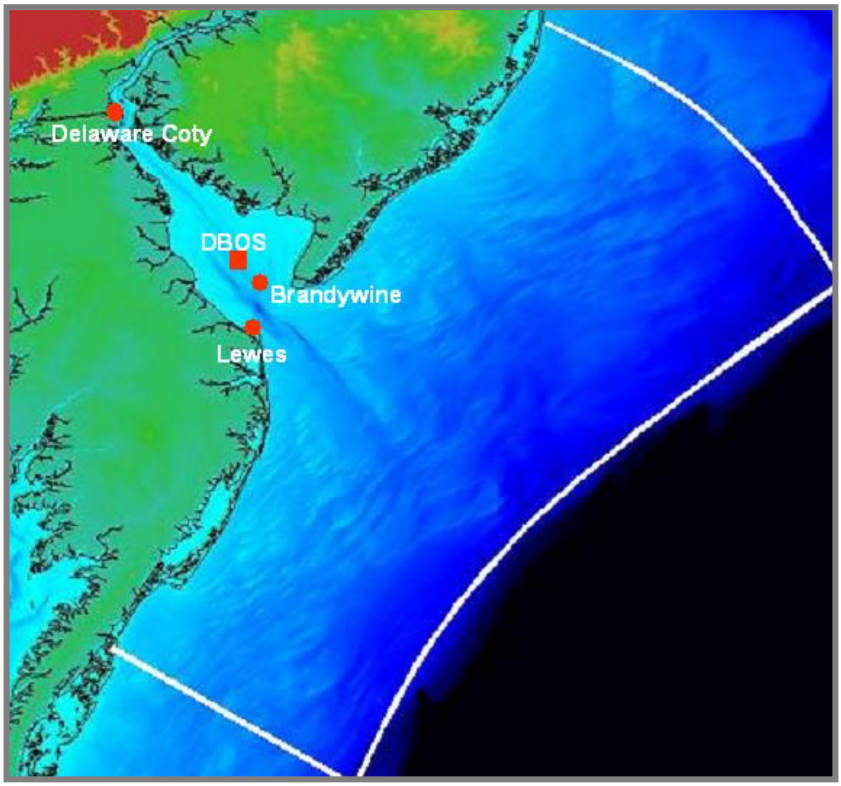

Figure 3.1: Computational domains for ROMS and SWAN

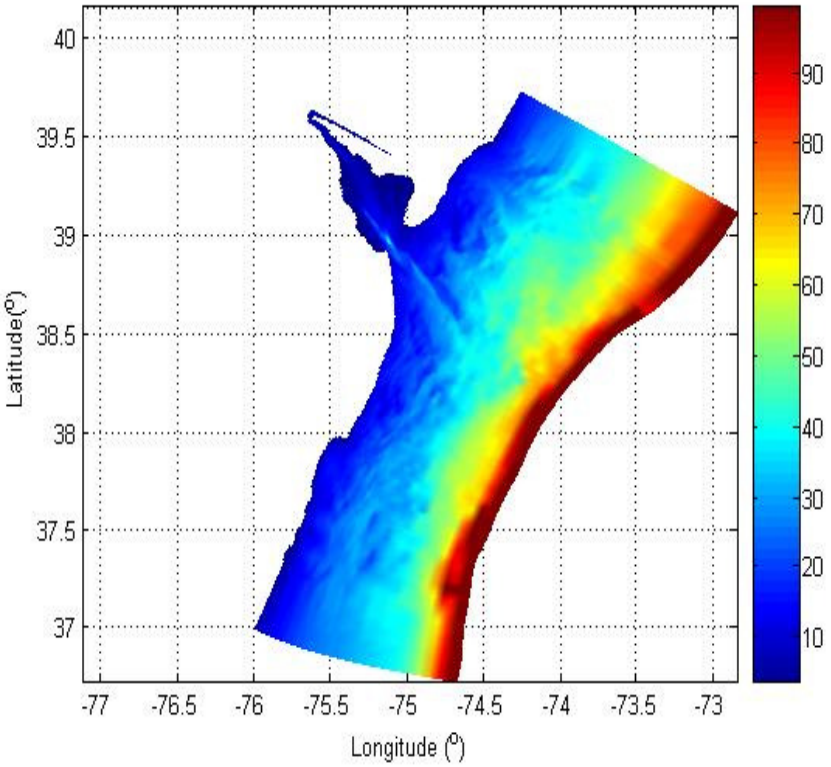

Figure 3.2: Bathymetry in Delaware Bay simulation.

(Unit in color bar is m)

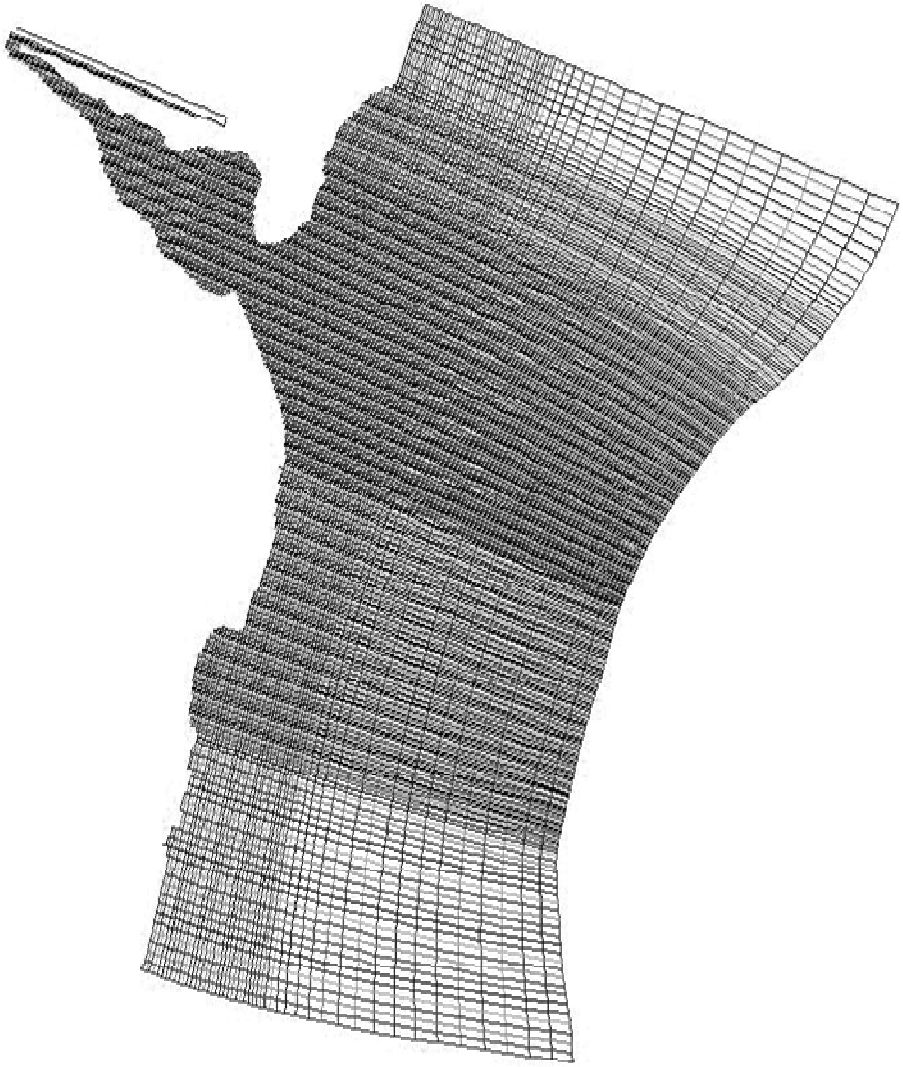

Figure 3.3: Computational grids for ROMS and SWAN

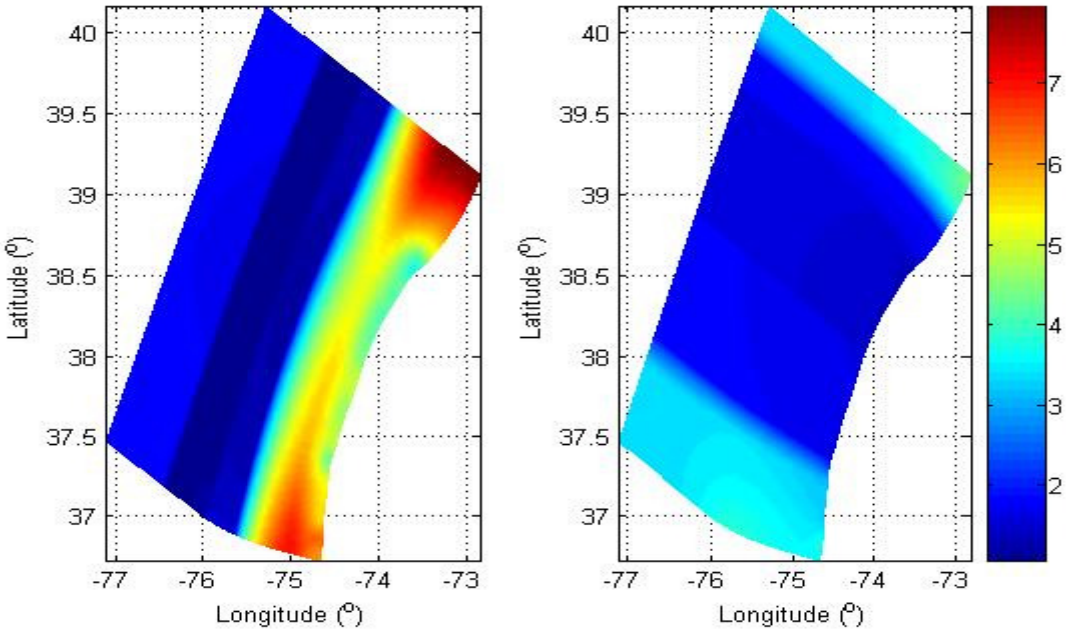

Figure 3.4: Grid cell size in longitude-direction (left panel) and latitude-direction (right panel) in Delaware Bay simulation

(Unit in color bar is km)

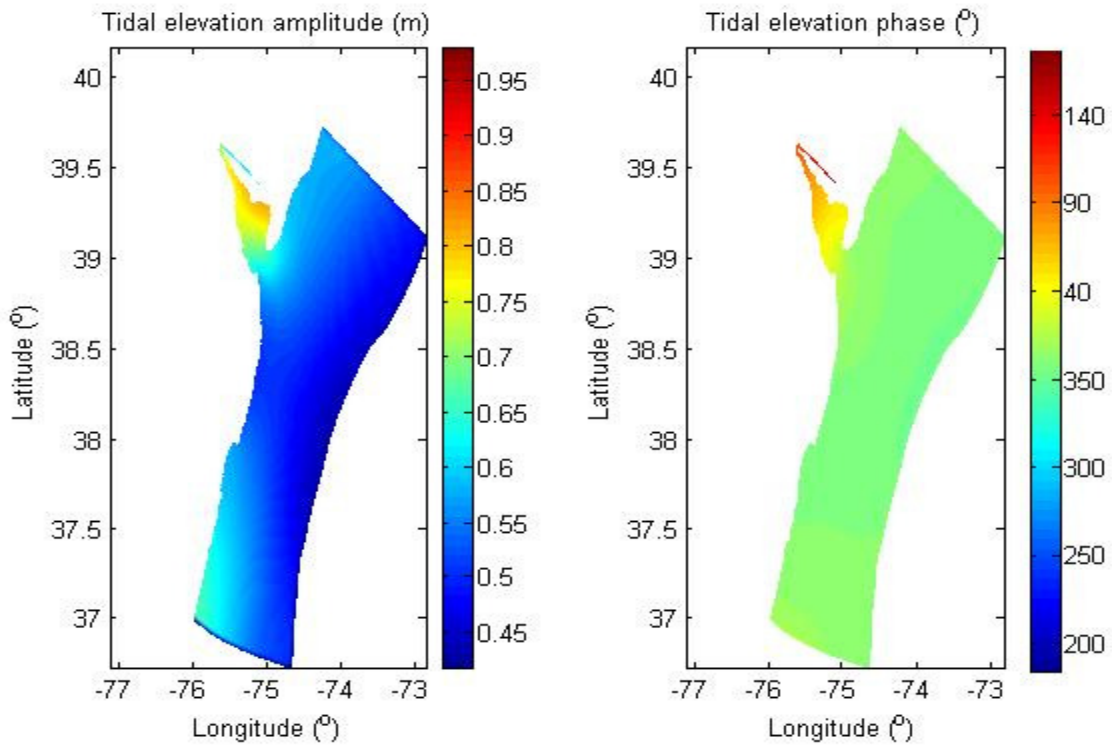

Figure 3.5: Tidal elevation simulation. Left Panel: Tidal elevation amplitude (m); Right Panel: Tidal elevation phase (^{o})

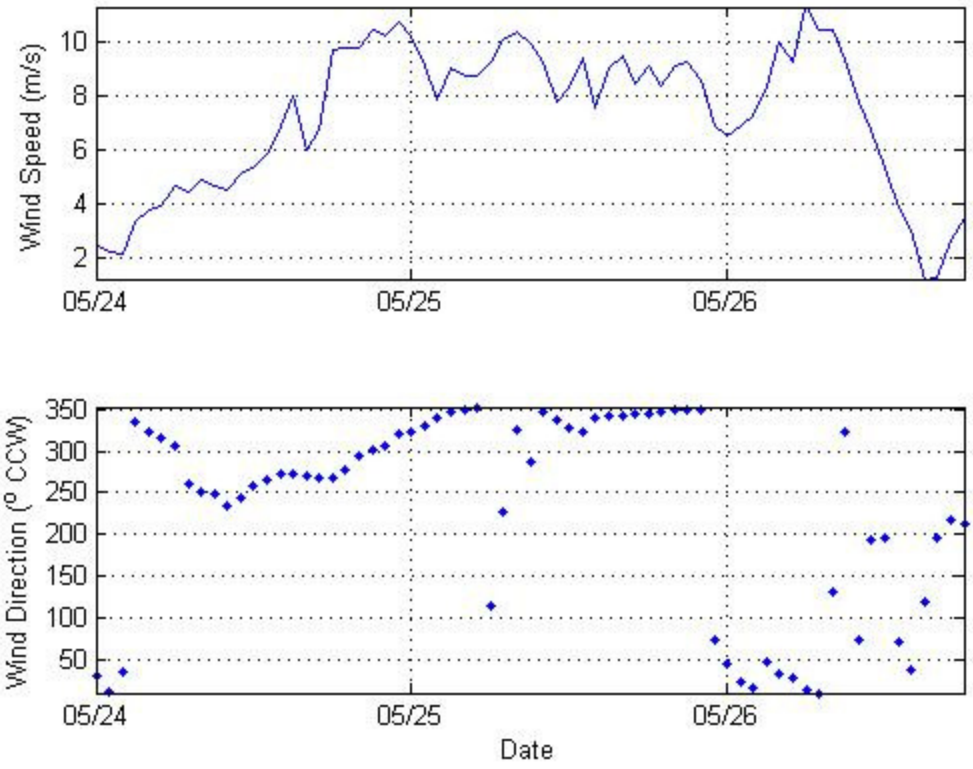

Figure 3.6: Recorded wind speed (upper panel) and direction (lower panel) at Fourteen Ft. Bank Lighthouse during 00:00 May 24 through 18:00 May 26, 2005

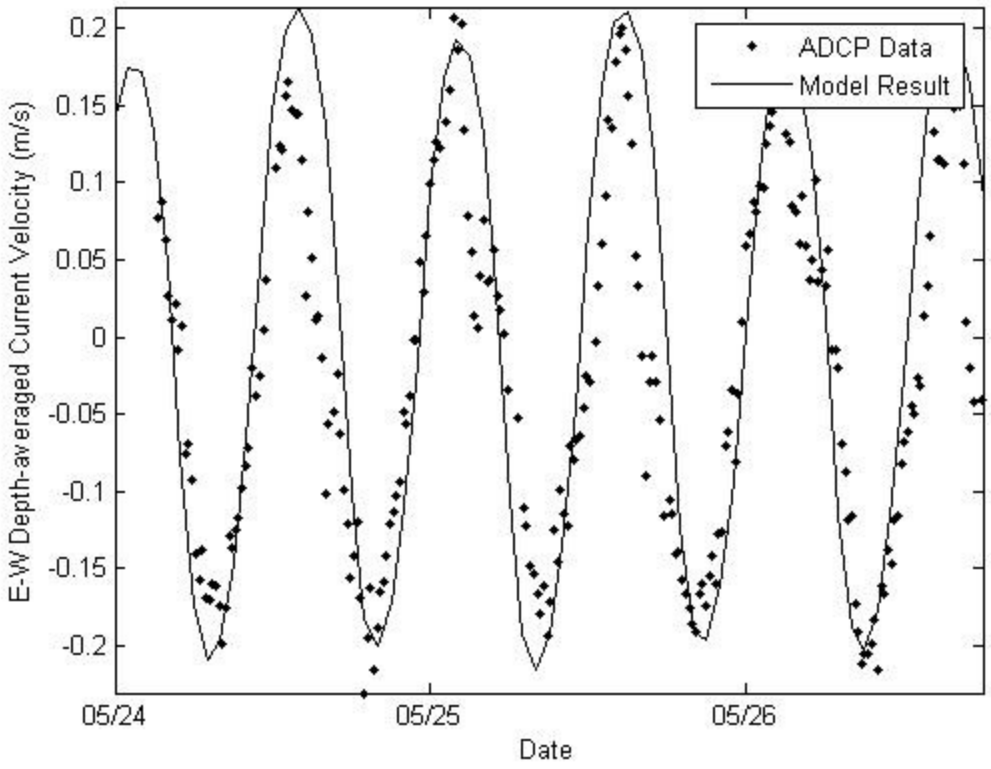

Figure 3.7: Comparison of E-W depth-averaged current velocity between ADCP measurement (dot) and numerical result (solid line) at Fourteen Ft. Bank Lighthouse in May, 2005

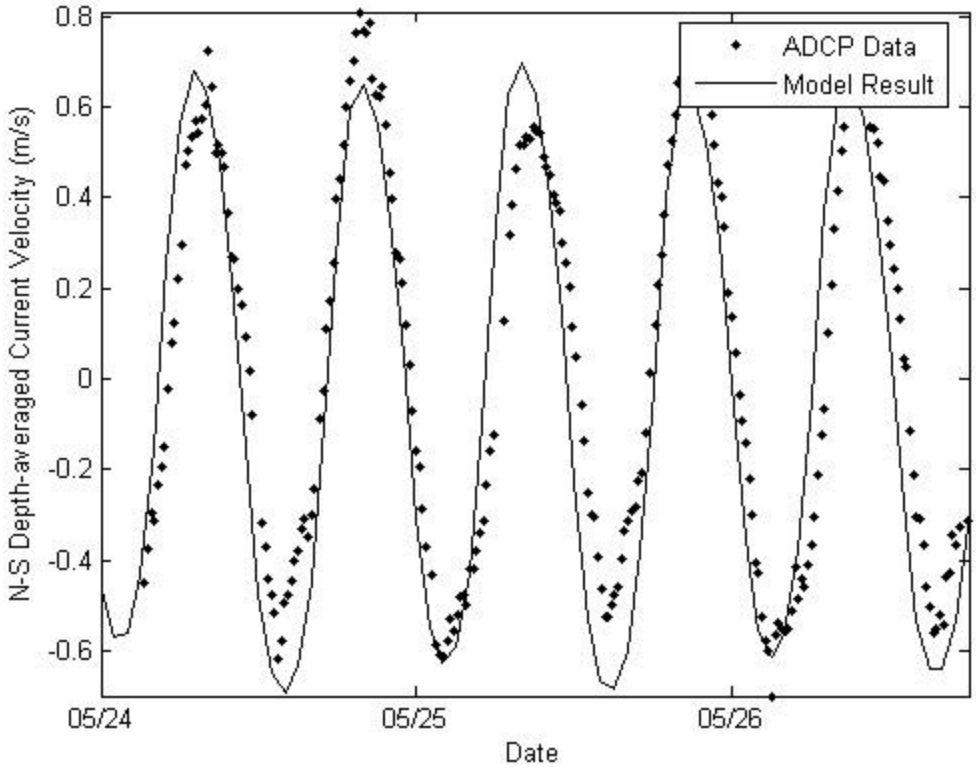

Figure 3.8: Comparison of N-S depth-averaged current velocity between ADCP measurement (dot) and numerical result (solid line) at Fourteen Ft. Bank Lighthouse in May, 2005

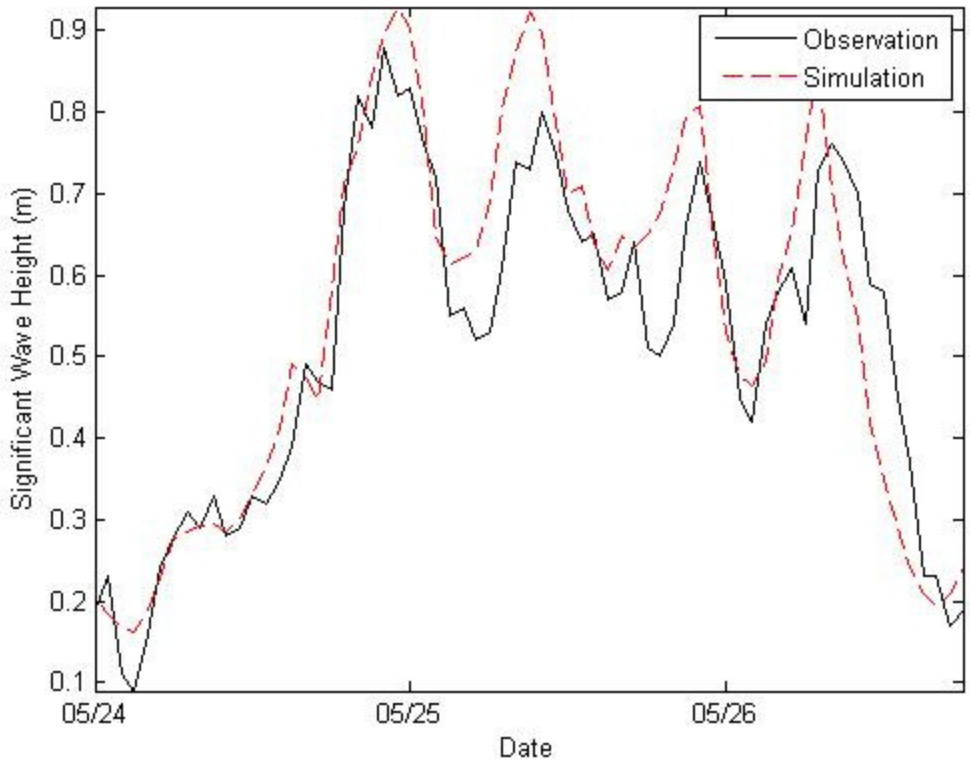

Figure 3.9: Comparison of significant wave height at Fourteen Ft. Bank Lighthouse during May 24 through May 27, 2005 between measured data at WSB (solid line) and numerical result (dash line)

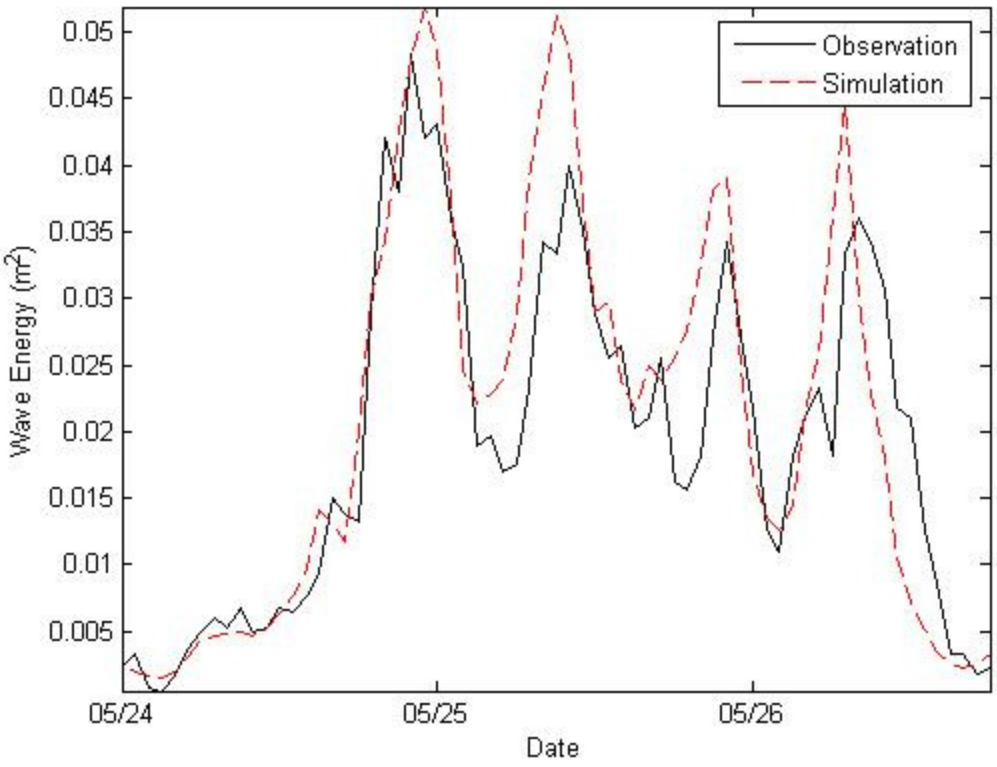

Figure 3.10: Comparison of wave energy at Fourteen Ft. Bank Lighthouse during May 24 through May 27, 2005 between measured data at WSB (solid line) and numerical result (dash line)

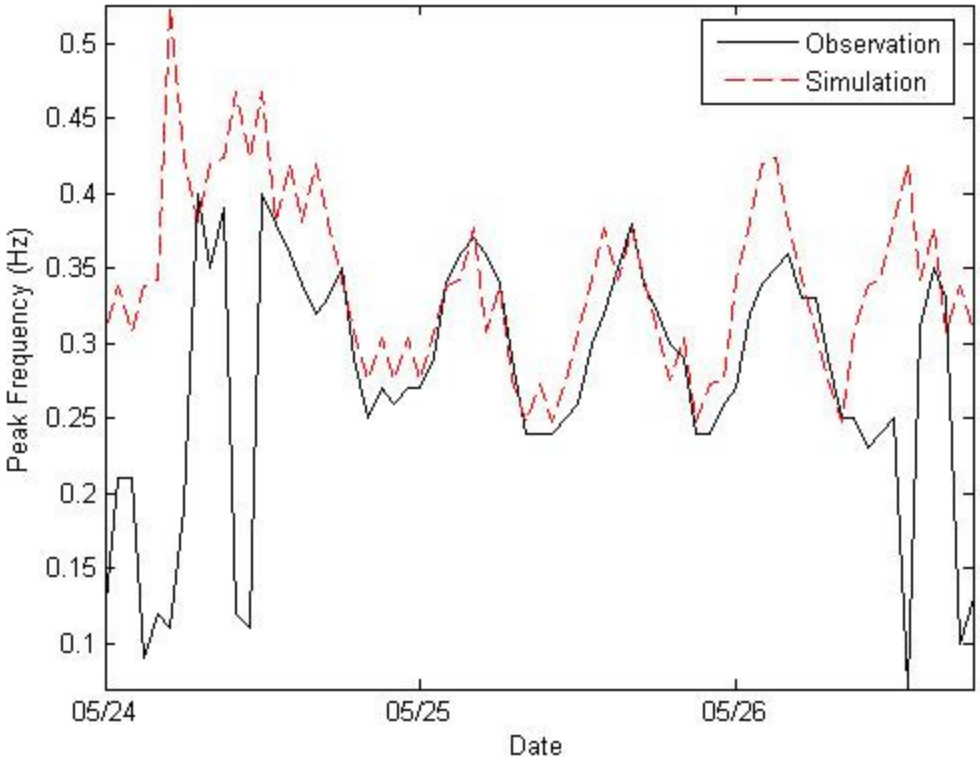

Figure 3.11: Comparison of peak frequency at Fourteen Ft. Bank Lighthouse during May 24 through May 27, 2005 between measured data at WSB (solid line) and numerical result (dash line)

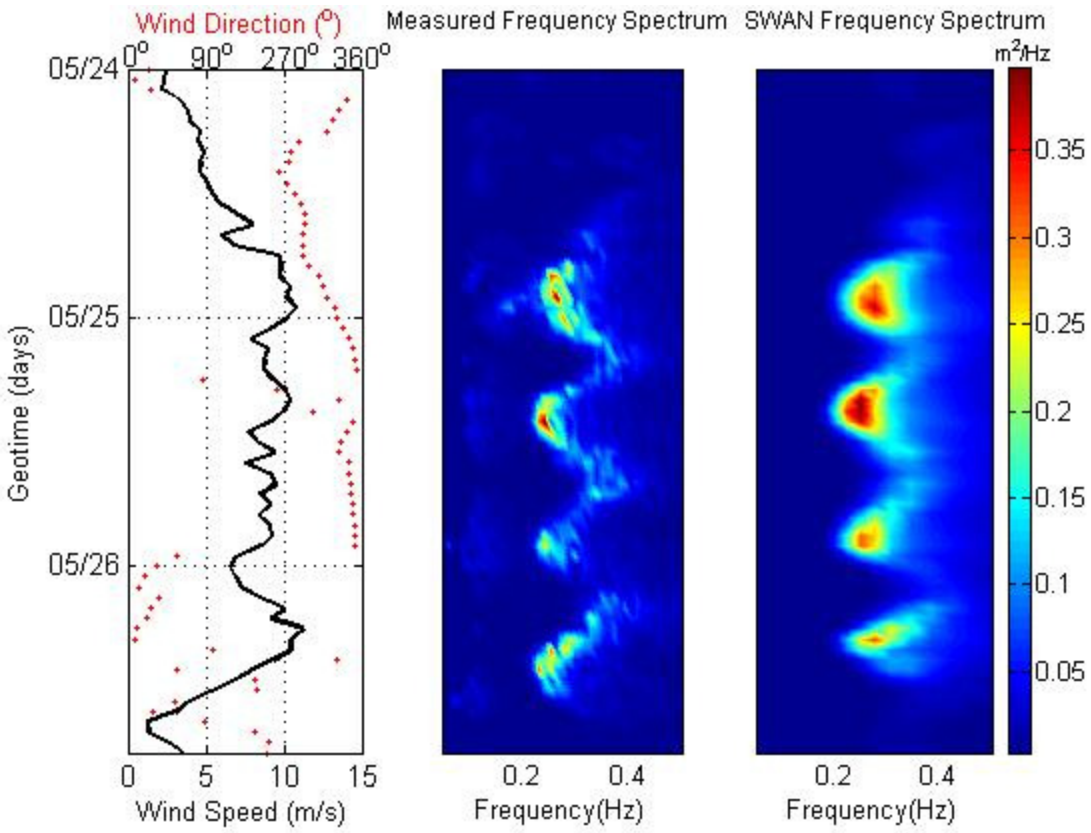

Figure 3.12: Left panel: Recorded wind speed (black solid line) and direction (red points, CCW) during May 24 through May 27, 2005 at Fourteen Ft. Bank Lighthouse; Middle panel: Frequency spectrum from WSB; Right panel: Frequency spectrum from model simulation.

Chapter 4

COASTAL INUNDATION INDUCED BY TROPICAL CYCLONES

Storm-induced surge, wave and inundation are believed to be sensitive to wave forcing and wind forcing. In this chapter, SWAN and SHORECIRC are coupled in the NearCoM system and are applied in a series of experiments for the purpose of investigating the response of storm surge and coastal inundation to wave forcing, as well as to cyclones through different atmospheric forcings on ocean surface. First, the model setup for those idealized experiments will be specified, including the model domain, model grids as well as wind field. After that, details of each experiment are specified, results and conclusions are presented.

4.1 Model Setup

For efficiency, the coupled SWAN/SHORECIRC system, instead of the coupled ROMS/SWAN system, is applied to idealized experiments to test the sensitivity of storm surge, waves and coastal inundation to the change of cyclone parameters. The experiments are carried out in an idealized, alongshore uniform domain which includes a planar beach, land and shelf with constant slopes.

4.1.1 Model Domain

The idealized computational domain is a rectangular region of 384.4 km across-shore and 1158.3 km along-shore with corresponding bathymetry of offshore boundary is along the 100 m isobath. It includes a planar beach with slope of 1/100, land and shelf with constant slope of 1/1000 as shown in Figure 4.1. The upper panel is the longitudinal profile of the entire domain and the lower panel is the longitudinal profile of part of the computational domain with details on the planar beach and shelf.

4.1.2 Model Grid

A stretched grid is applied for the rectangular domain as shown in Figure 4.2. The grids contains 150 × 722 cells covering about the 384.4 km × 1158.3 km area. The highest horizontal resolution is 80 m in the targeted flooding zone and 5 km off continental shelf. The lowest resolution is 8.8 km offshore. The target flooding zone is set to be -100 km to 100 km in the alongshore direction. In this way, grid number is greatly reduced for calculation while it can still be of enough resolution for modeling storm surges and wave heights as well as the flooding area. The grid cell sizes are shown in Figure 4.3. Left panel shows the grid cell size in cross shore direction and right panel shows the grid cell size in along shore direction. The color indicates the spacing in meter.

4.1.3 Wind Field

Parametric wind forcing is applied in the idealized experiments. Many parametric models have been developed for tropical cyclones wind studies (Holland,

1980; Harper and Holland, 1999; Vickery et al., 2000).

The coupled model system is driven by the surface kinematic wind stress which is applied at the sea surface boundary and the pressure gradient caused by atmospheric pressure is implemented as a body force in the model. The wind stress is evaluated using the conventional bulk formula:

$$\tau = \rho C_d \left|\vec{W}\right| W \tag{4.1}$$

where W is wind speed at height of 10 m; ρ is air density; C_d is the drag coefficient and are calculated by equation (4.2), which is widely used in storm surge modeling studies. It is different from the formulation used for SWAN in equation (2.59).

$$C_d \times 10^3 = \begin{cases} 1.052, & \left|\vec{W}\right| \le 6 m/s \\ 0.638 + 0.069\left|\vec{W}\right|, & 6 \le \left|\vec{W}\right| \le 30 m/s \\ 2.708, & \left|\vec{W}\right| \ge 30 m/s \end{cases} \tag{4.2}$$

The cyclone pressure p_a and wind velocity $\vec{W}$ were modeled following Holland (1980):

$$p_a = p_c + \Delta p \exp\left[-\left(\frac{r}{r_m}\right)^{-B}\right] \tag{4.3}$$

with $\Delta p = p_e - p_c$

where p_c is the central pressure of a cyclone and Δp is the pressure drop or deficit; B is the shape parameter; r is the distance from the cyclone center and r_m is the radius to maximum wind speed W_m. Wind velocity vector is calculated by a static wind profile W_c and an additional wind field associated with translation velocity:

$$\overrightarrow{W} = \begin{cases} W_c \dfrac{1}{r}(a\vec{i} + b\vec{j}) + W_T \dfrac{r}{r + r_m}, & r \le r_m \\ W_c \dfrac{1}{r}(a\vec{i} + b\vec{j}) + W_T \dfrac{r_m}{r + r_m}, & r \le r_m \end{cases} \tag{4.4}$$

where $a = -(x\sin\theta + y\cos\theta)$ and $b = x\cos\theta - y\sin\theta$, in which θ is the cyclone's inflow angle; and:

$$W_c = W_m \left[\gamma^B \exp(1 - \gamma^B) \right]^{1/2} \tag{4.5}$$

in which $\gamma = \dfrac{r_m}{r}$.

Additional surface boundary conditions in the form of heat, moisture and radiation fluxes can also be imposed, but are not used for the idealized experiments.

A series of hypothetical tropical cyclones are designed according to above parametric wind model in order to test the sensitivity of coastal flooding area, storm surge, wave height and flooding distances to different atmospheric forcings. The details of each experiment set-up will be presented later in each section of this chapter.

Parametric wind models should be significantly different between TC before and after landing. Only wind model before TC landing is designed in this study with focus on the duration before TC landing.

The coupled model system is run for about 30 hours, which is long enough for tropical cyclones to develop over the ocean, travel towards land and make land fall. In general, TC is designed to travel 20 hours before it lands. The wave model and circulation model exchange information at a time interval of 900 s.

4.2 Coastal Inundation Process Under Storm Conditions

Two specific inundation cases are presented with a set of time series snapshots of storm surges, waves as well as the wind fields. It shows clearly the movement of TC and the development of coastal inundation. All the snapshots are focused on the target area with -2000 m to 4000 m cross shore and -100 km to 100 km along shore. Both cases are carried out using NearCoM.

In the first case, the TC has a RMW of 40 km, MW of 70 m/s, translation speed of 5 m/s and incident angle of 150^{o}. Incident angle is defined in Cartesian coordinate as the angle from x direction to the travel direction of TC, counter-clock wisely, as shown in Figure 4.4. In this case, TC is traveling northwestward towards the land. Figure 4.5 shows four snapshots of storm surge (in color), flooded region (identified by the colored region on the left side of shoreline), as well as wind field (presented with vectors) at 5 hrs, 10 hrs, 15 hrs, and 20 hrs, respectively, and Figure 4.6 shows the corresponding snapshots of significant wave height. At the early stage of TC development (upper left panels in both Figure 4.5 and 4.6), it is still far away from the land. Basically most of the target domain is controlled by onshore wind field. The wind is blowing landward (only in the south part of the target domain where y is less than -90 km, it is controlled by offshore wind field with wind blowing seaward). Since the TC is still far away, the wind field is not strong, and both storm surges and waves are not apparent. As the TC is moving closer towards the land (from 5 hrs to 10 hrs, and then to 15 hrs and finally to 20 hrs), the wind field gets stronger, as indicated by the size of the vectors in Figure 4.5. Because TC is traveling northward in alongshore direction, more area in the

south part of the target domain is changing to be controlled by offshore wind field (but the upper half of the model domain is always controlled by onshore wind before TC landing). In the domain with onshore wind, the wind is blowing landward and piles the water onto land, and results in coastal inundation. In the domain with offshore wind, the wind is blowing seaward and tends to move the water away from the land. At 20 hrs (lower right panel in Figure 4.5), TC is landing at point of $x = 0$ and $y = 0$, the wind field becomes very strong, and whole upper half of the target domain is dominated by onshore wind. The wind blows strongly the water from ocean onto land and results in severe inundation. On the other hand, the whole lower half of the target domain is under control of offshore wind, which is associated with no (or small) inundated area. As the wind field becomes stronger (TC is closer to the land), the significant wave height is becoming larger as well as shown in Figure 4.6. Moreover, the wave height is decreasing with the decrease of water depth, indicating wave breaking nearshore as demonstrated in Figure 4.6.

In the second case, the TC is designed with the same wind parameters as in the first case, except the incident angle is 210^o, which indicates the TC moving northeastward towards land. Figure 4.7 and 4.8 are the time series snapshots of storm surge, wind field, coastal inundation and significant wave height. In this case, since the TC is moving towards land from northeast, originally almost the whole target model domain is controlled by weak offshore wind, as indicated in upper left panel in Figure 4.7. No (or small) area is inundated. As the TC moves closer towards the land, wind field is becoming stronger and, more area in the upper half target domain is to be under control

of onshore wind. The lower half of the target domain is always dominated by offshore wind before TC landing. Therefore, inundation occurs on the upper half of the target domain. At 20 hrs, when the TC lands at point of $x = 0$ and $y = 0$, the wind field becomes strongest, and results in strongest storm surge as well as coastal inundation (lower right panel in Figure 4.7). Figure 4.8 shows that with the movement of the TC, the wave is developing and transferring from north to south and becomes stronger and stronger. For both cases, however, at 20 hrs, the differences are found to be small.

4.3 Sensitivity Test

Storm-induced waves, surges and inundation are believed to be sensitive to wind forcing and wave forcing. In a study of storm surge and inundation in the Croatan-Albemarle-Pamlico estuary system, Peng et al. (2004) showed that, for a given storm track, if the lower minimum center pressure decreases or the radius of maximum wind (RMW) increases, the storm surge will increase and which will then produce more severe coastal inundation. However, the predicted inundation does not have a linear relationship with predicted surges. In this section, four factors: RMW, track of cyclones, MW and translation speed are investigated separately for influencing the storm surges and coastal inundation.

4.3.1 Radius of Maximum Wind (RMW)

RMW is an important parameter in the wind model that can influence TC induced storm surge (Peng et al., 2004). The RMW of an individual TC may be much

different from its intensity-based statistic value (Hsu and Yan, 1998). Large RMW not only increases wind duration for both onshore and offshore winds, but also increases wind fetch.

In order to test the influence of RMW on the storm surge and inundation, a set of experiments are carried out with RMW changing from 10 km to 110 km with an interval of 10 km. All other parameters of the parametric wind model are set to be of consistency throughout the experiments with incident angle of 150^{o}, MW of 70 m/s and translation speed of 5 m/s. All designed TC-s start and develop on ocean and travel towards land as long as 20 hours before landing. The duration before landing (the first 20 hours) is taken into consideration in this study because once the TC lands, it is strongly influenced by terrains.

Since wave setup has an important impact on surface elevation and coastal inundation, each experiment is carried out with two runs: one using model system with wave effects and the other one without wave effects.

Results of response of storm surges, inundations, waves and flooding distances to RMW are presented in Table 4.1 (with wave) and Table 4.2 (without wave).

Figure 4.9 presents the effect of RMW on the maximum storm surge through model system with wave effect (blue line) and without wave effect (red line). In general, the peak storm surge increases as RMW increases in both cases (with and without wave). The trend is nearly linear.

Concerning about the difference made by whether or not wave effect is considered in the system, Figure 4.9 shows obviously that peak storm surges predicted by

the system with wave effect are higher than those predicted by the system without wave effect. It is caused by wave-induced setup. The difference of the peak storm surges caused by wave-induced setup also increases with the increase of RMW.

Table 4.1: Experiment results of RMW

(with wave effect; incident angle: 150^{o}, MW: 70 m/s, translation speed: 5 m/s)

RMW (km)	Inundation areas (km^2)	Maximum flooding distance(m)	Maximum significant wave height (m)	Peak storm surge (m)
10	100.08	1080	7.4817	1.0608
20	139	1240	7.9167	1.2229
30	165.7575	1320	8.0584	1.3471
40	187.65	1480	8.1321	1.5077
50	207.805	1640	8.179	1.6549
60	222.7475	1720	8.2159	1.7478
70	233.52	1880	8.25	1.8684
80	240.8175	1960	8.2779	1.9448
90	245.335	1960	8.3016	1.9872
100	248.4625	1960	8.3339	1.9873
110	251.59	2040	8.3404	2.0633

Table 4.2: Experiment results of RMW

(without wave effect; incident angle: 150^{o}, MW: 70 m/s, translation speed: 5 m/s)

RMW (km)	Inundation areas (km^2)	Maximum flooding distance(m)	Peak storm surge (m)
10	52.125	680	0.6822
20	78.8825	840	0.8373
30	99.0375	920	0.9465
40	114.3275	1000	1.0287
50	127.5325	1080	1.1082
60	137.9575	1160	1.1805
70	145.255	1240	1.2416
80	151.51	1320	1.3035
90	154.6375	1320	1.3332
100	157.4175	1320	1.342
110	160.8925	1400	1.4014

Figure 4.10 shows the relationship between RMW and maximum flooding distance both with (blue line) and without wave effect (red line). The trend is similar to

that of the peak storm surge. Larger the RMW is, farther the flood will spread on land. Due to the wave-induced setup, the flood line moves farther on land when wave effect is considered in the model system than wave effect is not presented in the system. The difference increases with the increase of RMW.

Figure 4.11 presents the effect of RMW on the flooding area with wave effect (blue line) and without wave effect (red line). The flooding area is determined by the integration of the inundated grids on land. The grid is defined as inundated if the sea surface elevation on it is higher than the topography during the whole duration before TC landing for at least one time. Similar with the storm surge and flooding distance, the inundation area increases with the increase of RMW. The model with wave effect predicts a larger inundated area than the model without taking into account wave effect. The difference increases with the increase of RMW.

Figure 4.12 indicates the effect of RMW on the maximum significant wave height. Larger RMW also predicts larger significant wave height. The trend is not linear. For example, the increase in maximum significant wave height associated with increase of RMW from 10 km to 20 km is much larger than that associated with increase of RMW from 100 km to 110 km.

4.3.2 Track of Tropical Cyclone

Different tracks of TC-s can make significant differences in resulting coastal inundations, storm surges, significant wave heights as well as maximum flooding distances (Peng et al., 2004).

16 tracks of TC-s are designed with incident angles from 110^o to 250^o with an increment of 10^o. All other wind parameters are set to be RMW = 40 km, MW = 70m/s and translation speed = 5 m/s. Each experiment is carried out in two runs, one with wave effect, the other one without wave effect, to investigate the wave forcing effect.

Results are presented in Table 4.3 (with wave effect) and Table 4.4 (without wave effect).

Figure 4.13 presents the effect of TC track on the peak storm surge both with and without wave effect. Basically, in both cases (with and without wave effect), the largest peak storm surge occurs with the TC traveling towards land with an incident angle of around 180^o (it is 170^o for cases with wave effect and 190^o for cases without wave effect). For incident angles less than 180^o, the TC-s are traveling towards the land from southeast direction, the peak storm surge increases as the increase of incident angle; while for incident angles greater than 180^o, the peak storm surge decreases with the increase of incident angle.

Wave-induced setup always contributes in making larger peak storm surges at any incident angle as shown in Figure 4.16. The difference between model with wave effect and without wave effect also has a parabolic shape with the largest difference occurring at incident angle of 160^o.

Table 4.3: Experiment results of TC track

(with wave effect; RMW: 40 km, MW: 70m/s, translation speed: 5 m/s)

Angle (^{o})	Inundation areas (km^2)	Maximum flooding distance(m)	Maximum significant wave height (m)	Peak storm surge (m)
110	213.7125	1240	8.0003	1.2523
120	208.1525	1320	8.0316	1.3224
130	203.2875	1400	8.0707	1.4063
140	196.3375	1480	8.1083	1.4801
150	187.65	1480	8.1321	1.5077
160	178.615	1560	8.1337	1.5607
170	169.58	1560	8.1156	1.5648
180	160.545	1560	8.1128	1.563
190	153.595	1560	8.1027	1.5565
200	146.645	1480	8.0843	1.506
210	137.9575	1480	8.0567	1.4883
220	131.7025	1400	8.0133	1.4269
230	122.32	1400	7.9732	1.3975
240	112.9375	1320	7.8849	1.3276
250	110.505	1240	7.744	1.2626

Table 4.4: Experiment results of TC track

(without wave effect; RMW: 40 km, MW: 70m/s, translation speed: 5 m/s)

Incident Angle (^{o})	Inundation areas (km^2)	Maximum flooding distance(m)	Peak storm surge (m)
110	139	840	0.8693
120	131.7025	920	0.9129
130	126.49	1000	0.9697
140	120.93	1000	1.0057
150	114.3275	1000	1.0287
160	108.42	1080	1.0583
170	103.555	1080	1.0742
180	100.08	1080	1.0835
190	99.385	1080	1.0869
200	100.775	1080	1.0804
210	93.825	1080	1.0678
220	94.1725	1000	1.028
230	88.265	1000	1.0142
240	82.3575	1000	0.9967
250	82.36	920	0.9506

Figure 4.14 shows the how TC track affects the maximum flooding distance. The trend shares a similar parabolic shape with that of peak storm surge. The largest maximum flooding distance occurs associated with the incident angle of around 180^o. However the trend lines are less smoother, which may indicate that the computational grid is not fine enough to resolve the shoreline movement induced by small elevation changes. Wave-induced setup resulted in larger maximum flooding distance, again, for all incident angles, as shown in Figure 4.14.

Figure 4.15 demonstrates the relationship between incident angle and maximum significant wave height. The largest significant wave height (8.13 m) occurs at angle of 160^o. Maximum significant wave height increases with the increase of incident angle when incident angles are less than 160^o, and the trend is opposite for incident angles greater than 160^o.

Different from the effect of incident angle on peak storm surge, maximum flooding distance and significant wave height, the inundated area generally decreases with the increase of the incident angle as shown in Figure 4.16. The reason is when the TC travels from southeast, the wind field helps in creating longer duration of, and hence worse, inundation at the target area. The model with wave effect always predicts larger and more severe inundation because of wave setup. The comparison between Figure 4.13 and Figure 4.16 reveals that larger peak storm surge does not necessarily correspond to more severe coastal inundation in the model domain. A larger peak storm surge may correspond to a local severe inundation, which is demonstrated by Figure 4.17 and Figure 4.18. Comparison between incident angles of 100^o and 180^o (either in Figure 4.17 or in

Figure 4.18) shows that the maximum flooding distance associated with 180^o is larger while the inundated area associated with 100^o is larger.

It should be mentioned that, by comparing the results for incident angle experiments to those for RMW experiments, the difference in peak storm surges caused by different angles is much smaller than those caused by different RMW-s, while for the differences in inundation area caused by different angles and by different RMW-s are closer. For detailed and quantitative comparisons, we define relative percent difference as:

$$Diff = \frac{|x1 - x2|}{(x1 + x2)/2} * 100\% \tag{4.6}$$

where, $x1$ and $x2$ are two positive values.

Table 4.5 shows the RPD for both RMW and TC track experiments. Basically, both peak storm surge and inundation area are very sensitive to RMW. As for incident angle, the peak storm surge is less sensitive compared with RMW. Although incident angle does not make very big difference in peak storm surge, it does result in much bigger difference in inundation area.

Table 4.5: Relative Percent Difference for RMW and TC Tract Experiments

	Peak Storm Surge		Inundation Area	
	With Wave	Without Wave	With Wave	Without Wave
RMW Test	64.18%	69.03%	86.17%	102.12%

Angle Test	22.19%	22.25%	63.67%	51.17%

4.3.3 Maximum Wind Speed (MW)

MW is another parameter that affects TC-induced inundation. A series of experiments with MW ranging from 30 m/s to 110 m/s with an increment of 10 m/s are conducted to examine the influence of MW. All other wind parameters are set to be the same throughout the experiments with RMW of 40 km, incident angle of 150^{o} and translation speed of 5 m/s. Each experiment is carried out with two runs, one with wave effect and the other one without wave effect.

Table 4.6 shows the results when wave effect is considered in the system and Table 4.7 shows the results without wave effect.

The response of peak storm surges to MW is presented in Figure 4.19. With the increase of MW, the peak storm surge also increases. System with wave effect predicts larger peak storm surge because of wave-induced setup. Figure 4.20 shows the relationship between maximum flooding distance and MW. It shares similar trend with that of peak storm surge: larger MW results in larger maximum flooding distance. Similarly, the relationship between inundation area and MW is shown in Figure 4.21, which indicates that the increase of MW results in the increase of inundation area, and wave-setup contributes in making more server inundation. Maximum significant wave height increases when MW increases as shown in Figure 4.22. The trend is not linear: the increase in maximum significant wave height associated with MW increases from 30 m/s

to 40 m/s is much larger than that associated with MW increases from 100 m/s to 110 m/s.

Inundation area and peak storm surge are very sensitive to MW with large RPD value of 158.5% and 143.7% for the case with wave effect, respectively, and 179.4% and 165.9% for the case without wave effect, respectively.

Table 4.6: Experiment results of MW

(with wave effect; RMW: 40 km, incident angle: 150^{o}, translation speed: 5 m/s)

MW (m/s)	Inundation areas (km^2)	Flooding Distance(m)	Significant wave height (m)	Peak storm surge (m)
30	62.55	440	4.9288	0.4348
40	91.3925	600	6.5998	0.6357
50	121.625	840	7.4947	0.8641
60	152.205	1080	7.8813	1.1104
70	187.65	1480	8.1321	1.5077
80	235.2575	2040	8.3355	2.0629
90	288.7725	2760	8.5167	2.7566
100	341.94	3000	8.6873	3.3326
110	381.9025	3000	8.8585	3.7556

Table 4.7: Experiment results of MW

(without wave effect; RMW: 40 km, incident angle: 150^{o}, translation speed: 5 m/s)

MW (m/s)	Inundation areas (km^2)	Flooding Distance(m)	Peak storm surge (m)
30	27.8	200	0.1873
40	45.5225	280	0.3048
50	63.245	440	0.4736
60	86.18	680	0.7096
70	114.3275	1000	1.0287
80	150.4675	1480	1.4808
90	193.5575	2040	2.0618
100	245.335	2840	2.8471
110	298.155	3000	3.4436

4.3.4 Translation Speed

Translation speed is another factor that can affect the storm surges and coastal inundation area (Pent et al., 2004). The sensitivity of storm surge to storm translation

speed can be vastly different for different storms. A set of experiments with different translation speed changing from 2 m/s to 13 m/s with an equal unit changing of 1 m/s. All other wind parameters are set to be the same throughout the experiments, with RMW of 40 km, MW of 150^{o}, MW of 70 m/s. All the storms are designed to start to develop at the same location indicating duration before TC landing for those storms with larger translation speed is shorter than those with smaller translation speed. Each experiment is carried out using two models, one with wave effect and one without wave effect.

Table 4.8 is the results for model with wave effect and Table 4.9 shows the results without wave effect.

Different from the results presented by Peng et al. (2004), the response of peak storm surges to translation speed is not monotonously decreasing, as shown in Figure 4.23. The relative percent difference for peak storm surge, are 20.04% for the case with wave effect, and 35.17% for the case without wave effect. They are much smaller compared with RMW and MW experiments, indicating that peak storm surge is not sensitive to translation speed compared with other factors. One of the possibilities might be that the coastline is straight and water pile-up effect is not obvious. For more complicated and realistic coasts and bays, storms with a longer duration would make water pile-up locally, resulting in a larger storm surge such as in the cases described in Peng (2004). In the idealized study, however, because of the straight open coast in the large domain, pile-up of ocean water is not obvious. Water spread fast, leading to small difference of peak storm surge between long and short duration of storms.

Figure 4.24 shows the effect of translation speed on maximum flooding

distance, which shares the similar pattern with peak storm surge.

Figure 4.25 demonstrates the relationship between flooding area and storm speed. Different from the results of Peng et al., the pattern is not monotonously decreasing. The reason is the same as explained for the peak storm surge. The relative percent differences for flooding area are 8.97% for the case with wave effect and 22.10% for the case without wave effect, respectively. In both cases, the values are much smaller than those for RMW and MW test, indicating that inundation area in this idealized experiment is not sensitive to translation speed compared with other factors.

Table 4.8: Experiment results of Translation Speed

(with wave effect; RMW: 40 km, MW: 150^{o}, MW: 70 m/s)

Speed (m/s)	Inundation areas (km^2)	Flooding Distance(m)	Significant wave height (m)	Peak storm surge (m)
4	194.2525	1640	8.1555	1.6255
5	187.65	1480	8.1321	1.5077
6	185.9125	1480	8.1047	1.4949
7	187.9975	1560	8.1145	1.5859
8	189.735	1720	8.0686	1.7019
9	190.7775	1800	8.0615	1.8119
10	189.3875	1800	8.0013	1.8279

11	181.7425	1720	7.8915	1.7505
12	177.5725	1720	7.7577	1.7282

Table 4.9: Experiment results of Translation Speed

(without wave effect; RMW: 40 km, MW: 150^{o}, MW: 70 m/s)

Speed (m/s)	Inundation areas (km^2)	Flooding Distance(m)	Peak storm surge (m)
4	123.015	1080	1.1089
5	114.3275	1000	1.0287
6	111.895	1000	0.9898
7	120.235	1080	1.0827
8	129.6175	1160	1.1821
9	137.61	1320	1.3483
10	139.695	1400	1.4122
11	137.61	1400	1.3994
12	138.305	1400	1.4071

Figure 4.26 shows the results for maximum significant wave height. Maximum significant wave height decreases with the increase of translation speed. The reason is that larger translation speed indicating shorter duration of the storm in this

study, and thus smaller maximum significant wave height.

4.4 Summary

Four factors: RMW, track of TC-s, MW and translation speed, in wind model are investigated for affecting the storm surges and inundation. The effect of wave-current interaction to the inundation is tested as well through a series idealized experiments. Numerical results indicate that, generally, larger RMW or larger MW will result in larger storm surge and larger coastal inundation area. As for the track of TC, lager incident angle predicts larger coastal inundation. However, the largest storm surge occurs at the incident angle around 180^{o}, indicating TC travels westward towards the land. Wave forcing is also an important factor in affecting the coastal inundation. Basically, when wave effect is presented in the model system, it predicts larger storm surge, flooding distance and more severe coastal inundation due to the wave-induced setup. As for translation speed, it is found to be of less importance in this study. One possibility is water pile-up vanishes in the idealized straight coast domain.

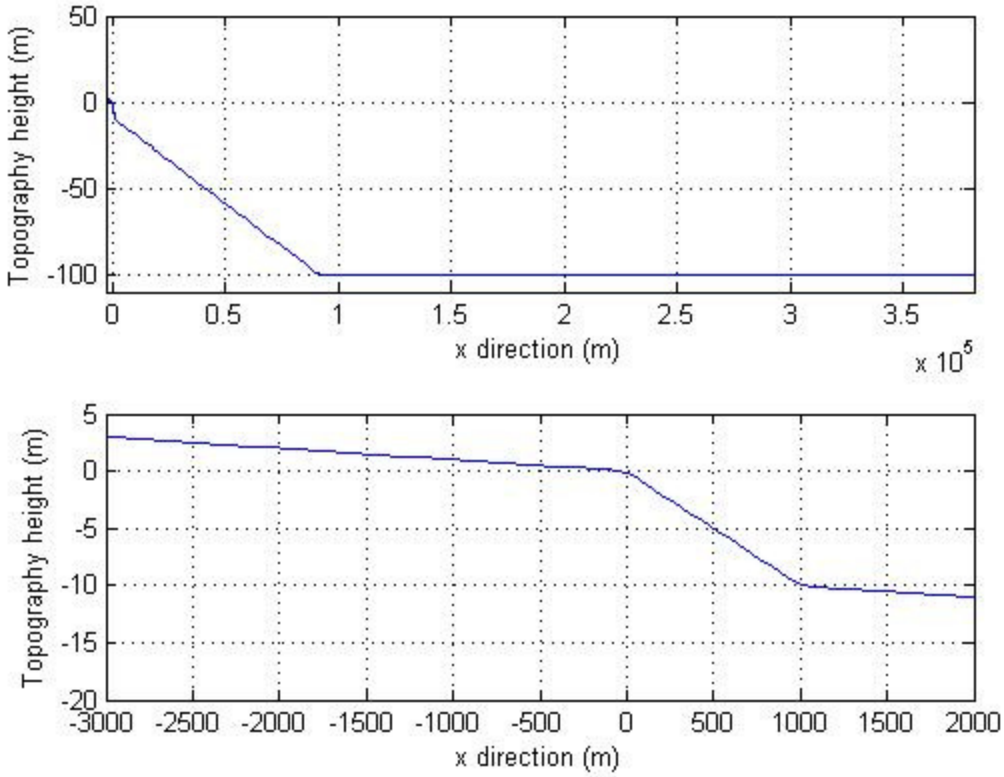

Figure 4.1: Longitudinal profile of the entire idealized model domain (upper panel) and part of the model domain with focus on the planar beach and shelf (lower panel)

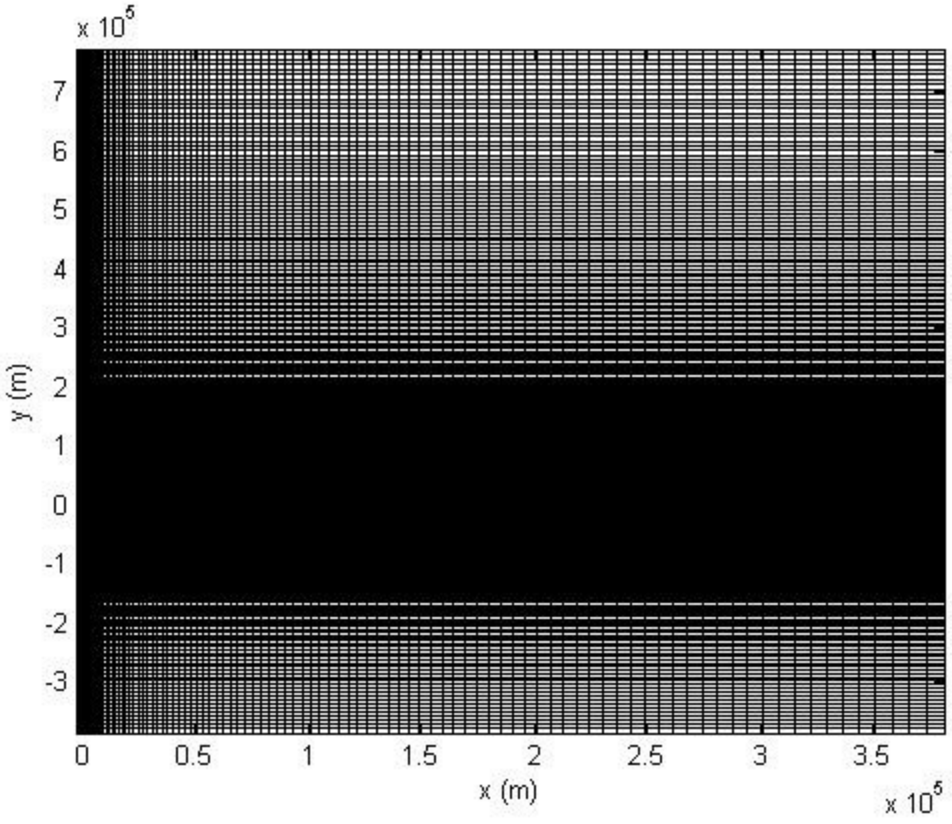

Figure 4.2: Grid cells in the idealized model domain

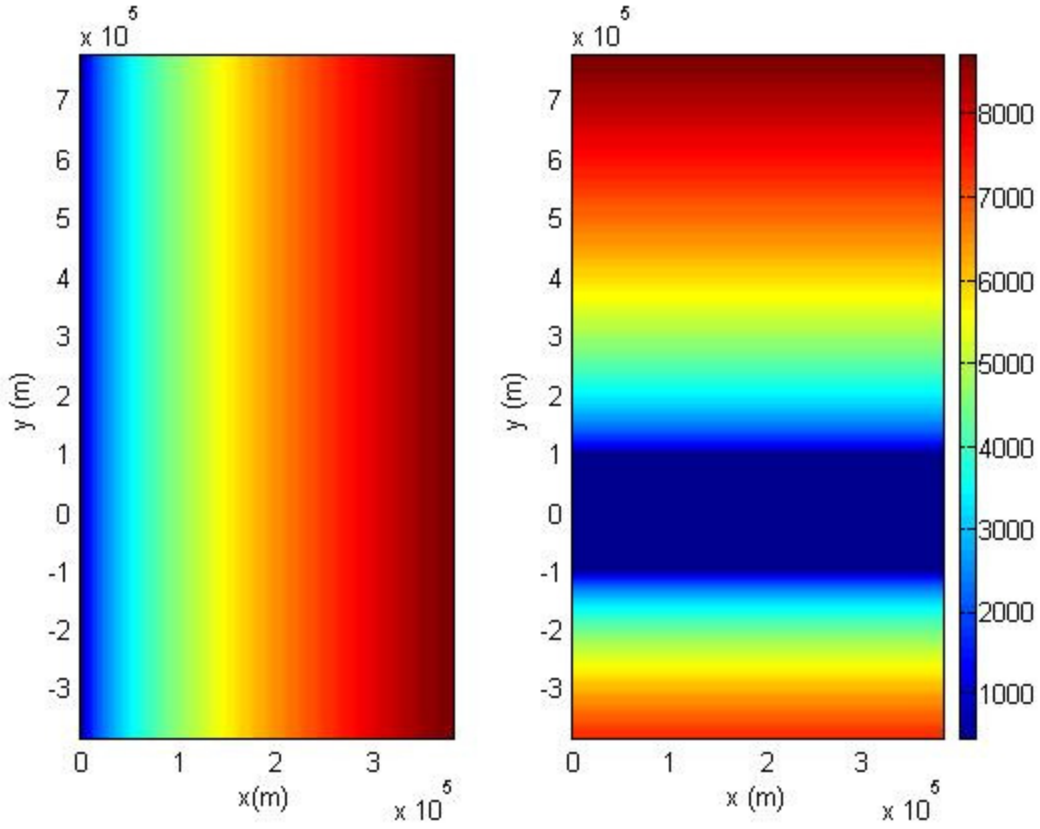

Figure 4.3: Grid cell size in x-direction (left panel) and y-direction (right panel)

(Unit in color bar is m)

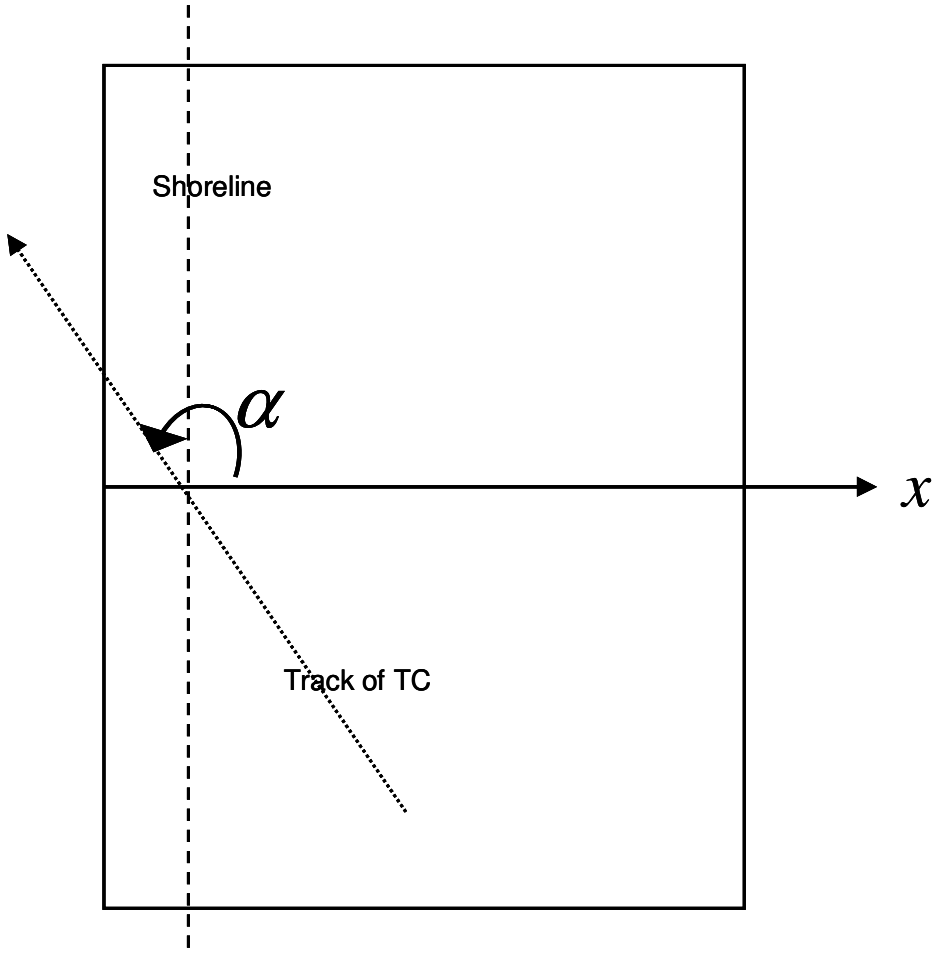

Figure 4.4: Sketch of incident angle α

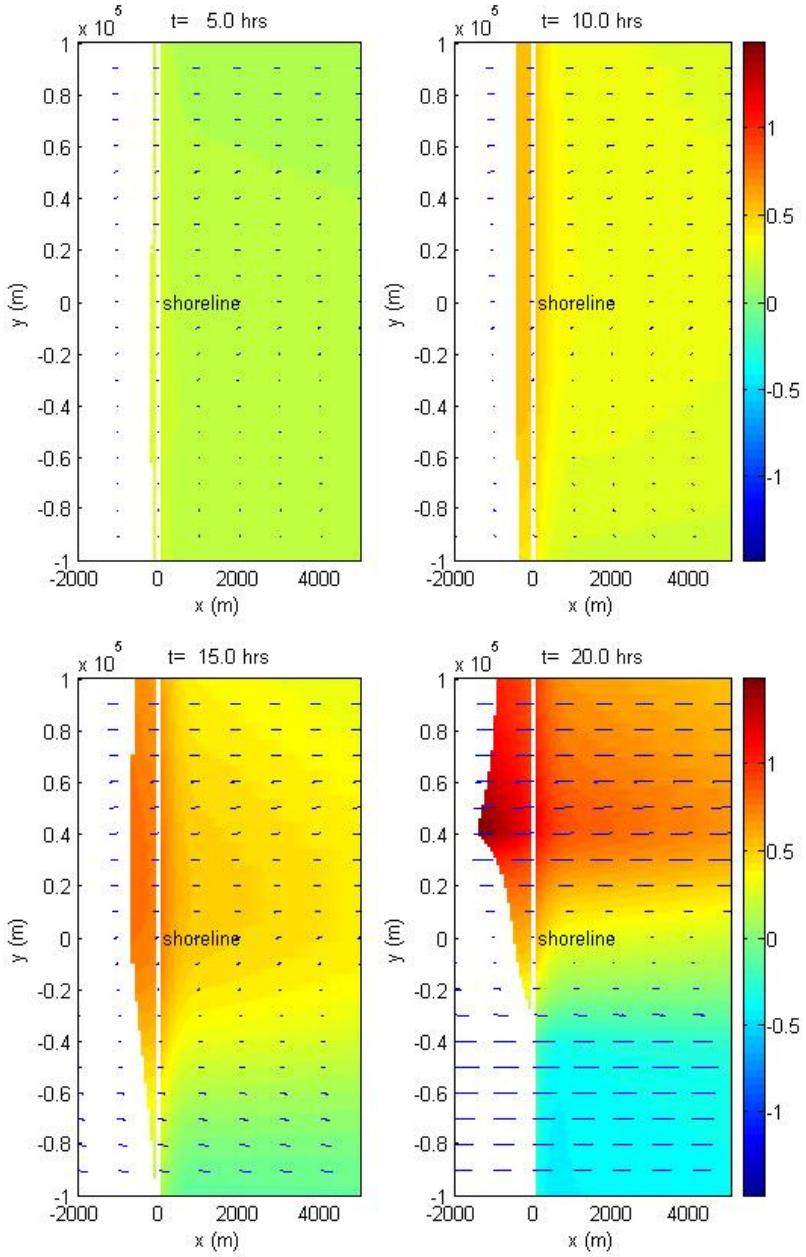

Figure 4.5: Snapshots of surge (color), flooded region (colored area on the left side of shoreline), and wind field (vectors) with incident angle of 150^{o} at 5 hrs (upper left panel), 10 hrs (upper right panel), 15 hrs (lower left panel), and 20 hrs (lower right panel) (Unit in color bar is m)

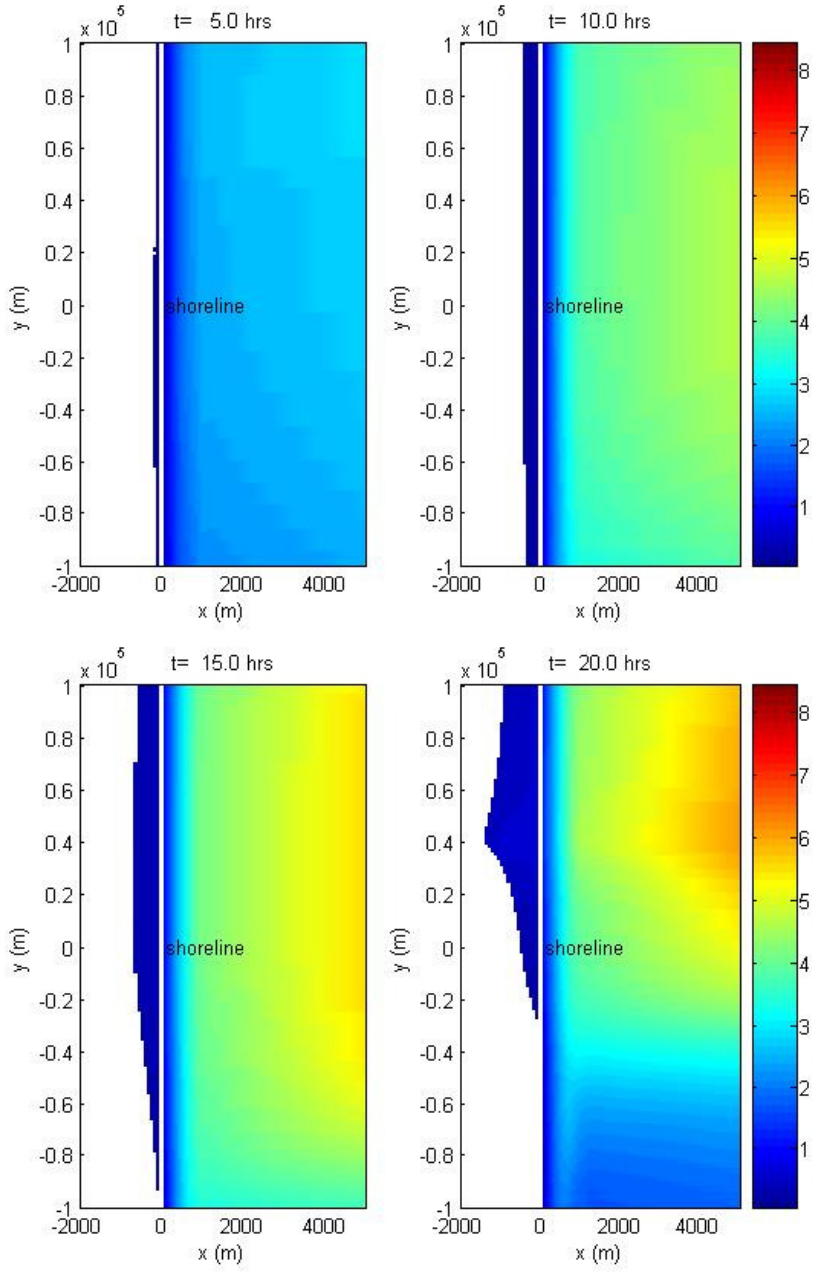

Figure 4.6: Snapshots of significant wave height with incident angle of 150^{o} at 5 hrs (upper left panel), 10 hrs (upper right panel), 15 hrs (lower left panel), and 20 hrs (lower right panel) (Unit in color bar is m)

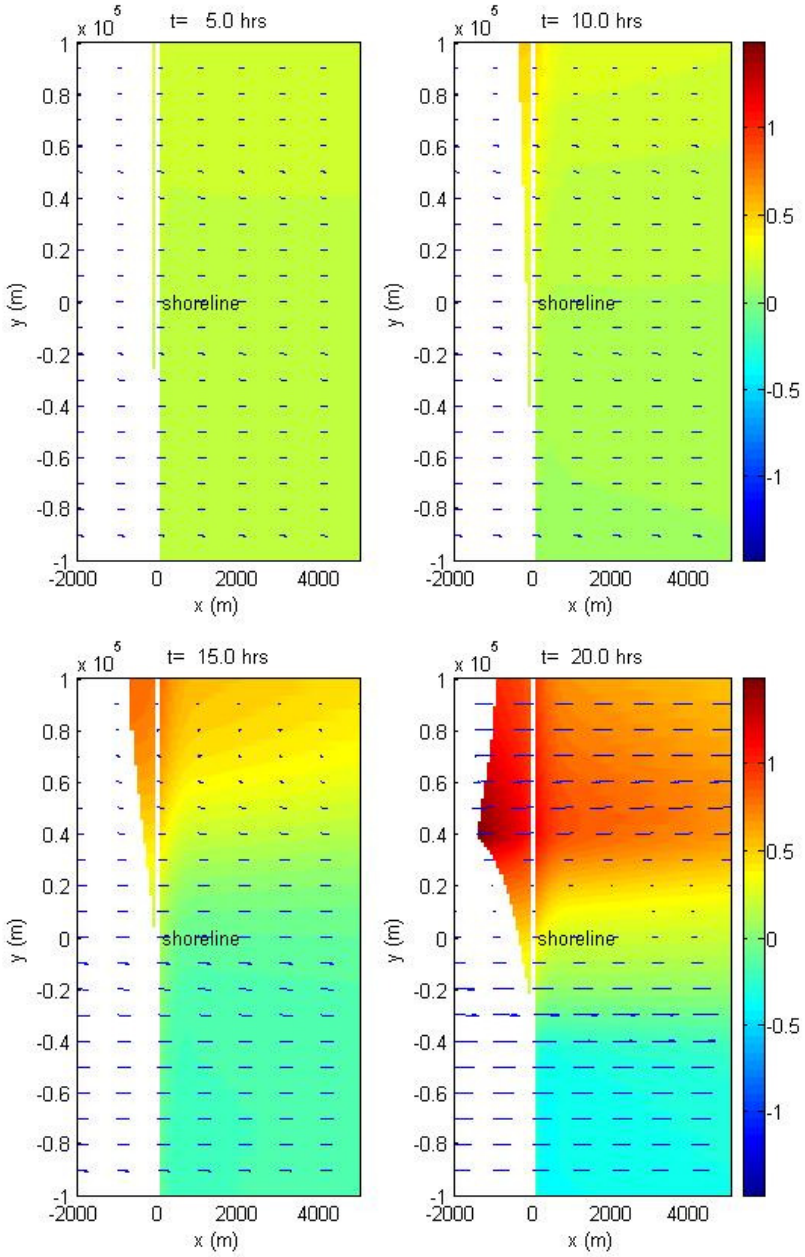

Figure 4.7: Snapshots of surge (color), flooded region (colored area on the left side of shoreline) and wind field (vectors) with incident angle of 210^{o} at 5 hrs (upper left panel), 10 hrs (upper right panel), 15 hrs (lower left panel), and 20 hrs (lower right panel) (Unit in color bar is m)

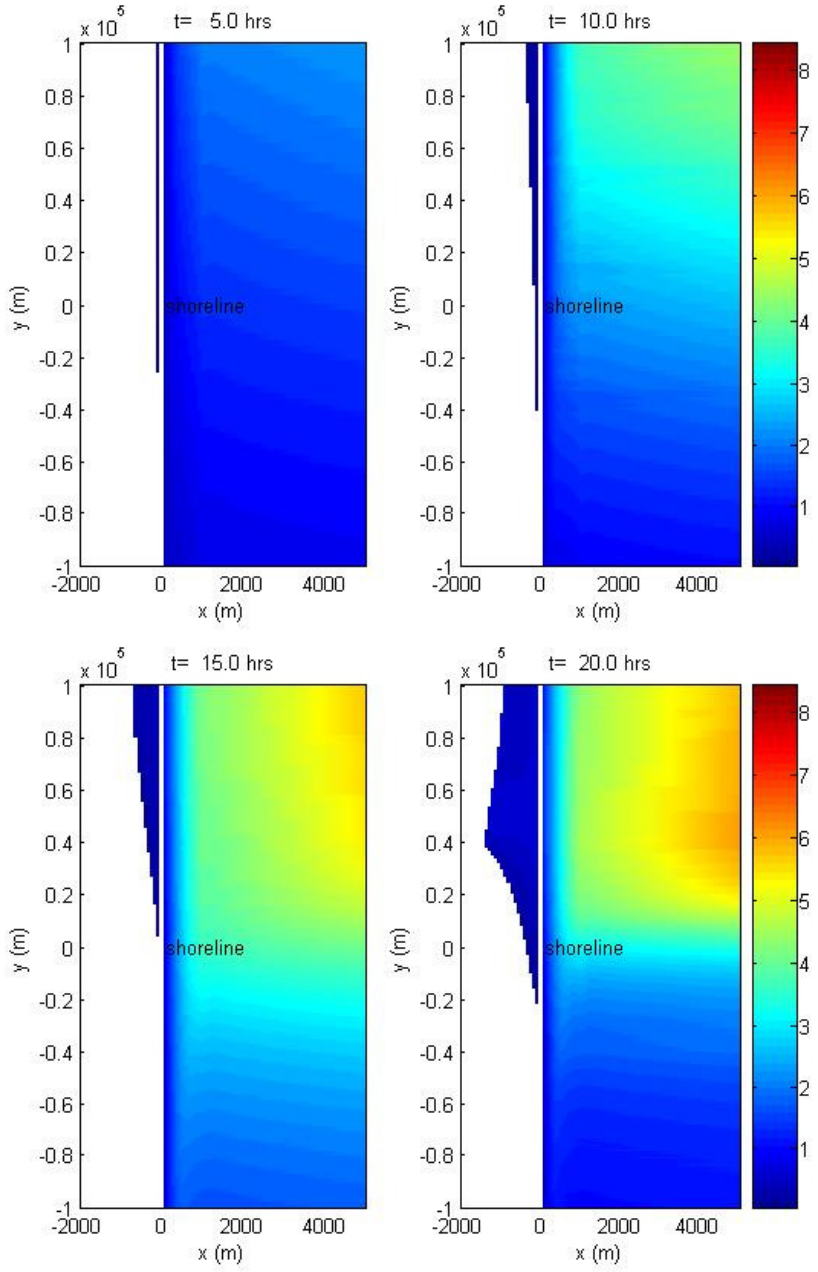

Figure 4.8: Snapshots of significant wave height with incident angle of 210^{o} at 5 hrs (upper left panel), 10 hrs (upper right panel), and 15 hrs (lower left panel), and 20 hrs (lower right panel)(Unit in color bar is m)

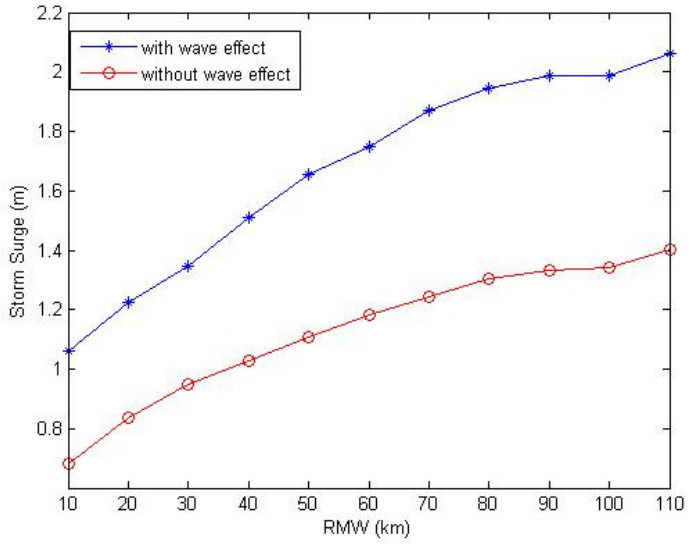

Figure 4.9: The effect of RMW on peak storm surge using model with wave effect (blue line) and without wave effect (red line)

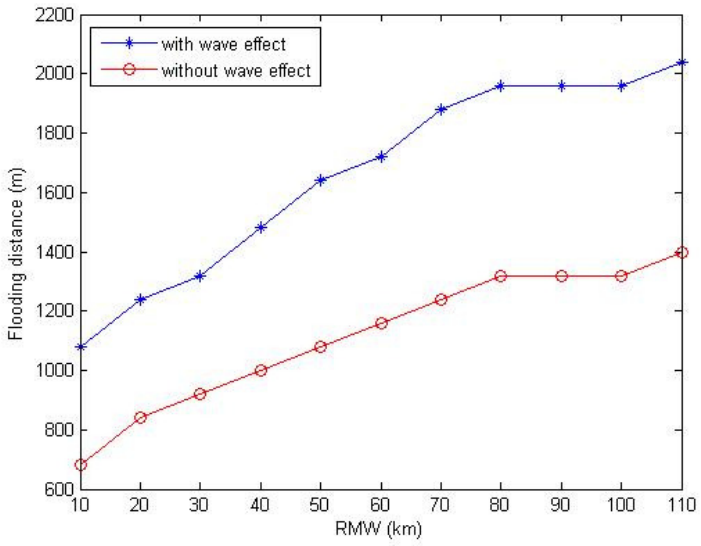

Figure 4.10: The effect of RMW on maximum inundation distance using model with wave effect (blue line) and without wave effect (red line)

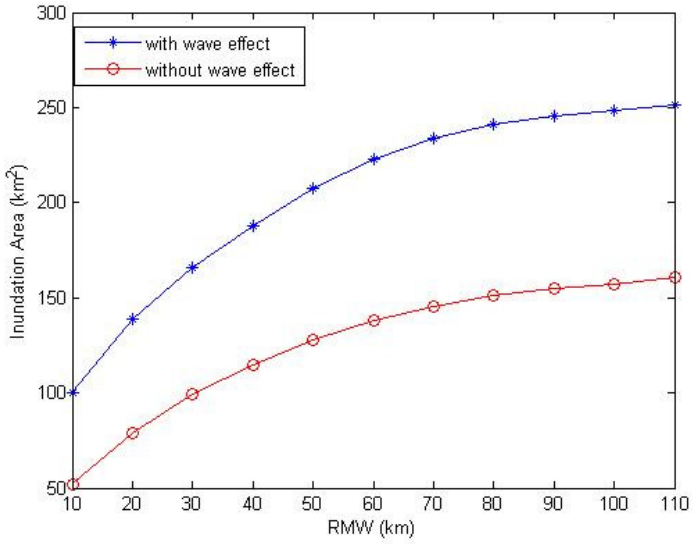

Figure 4.11: The effect of RMW on inundation area using model with wave effect (blue line) and without wave effect (red line)

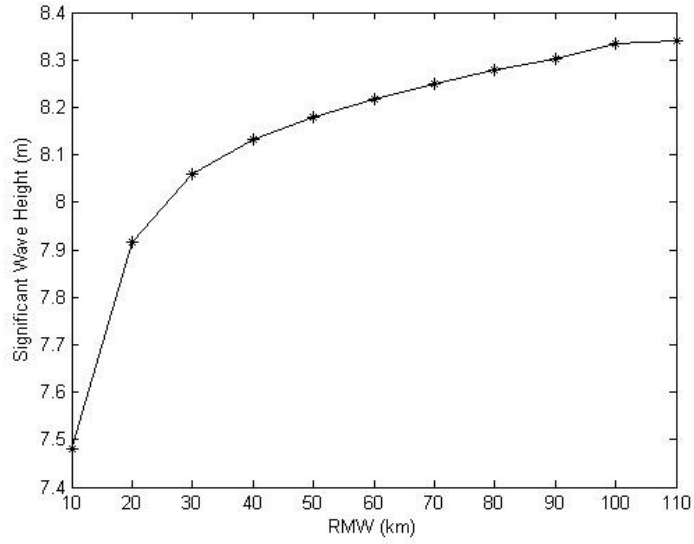

Figure 4.12: The effect of RMW on significant wave height using model with wave effect

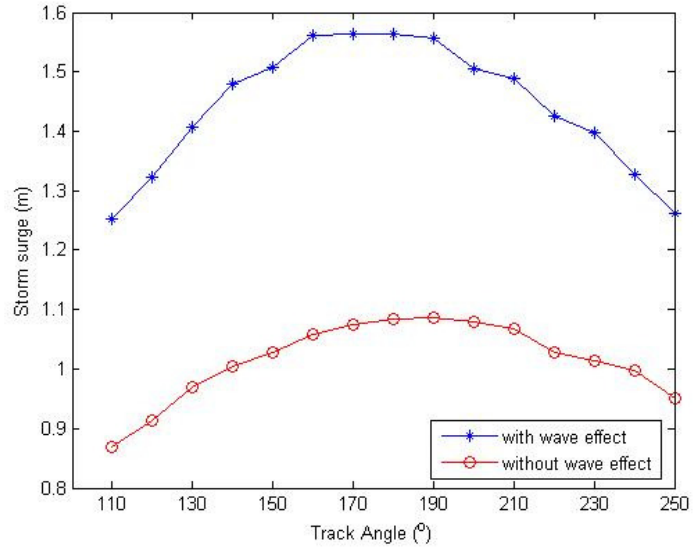

Figure 4.13: The effect of TC track on peak storm surge using model with wave effect (blue line) and without wave effect (red line)

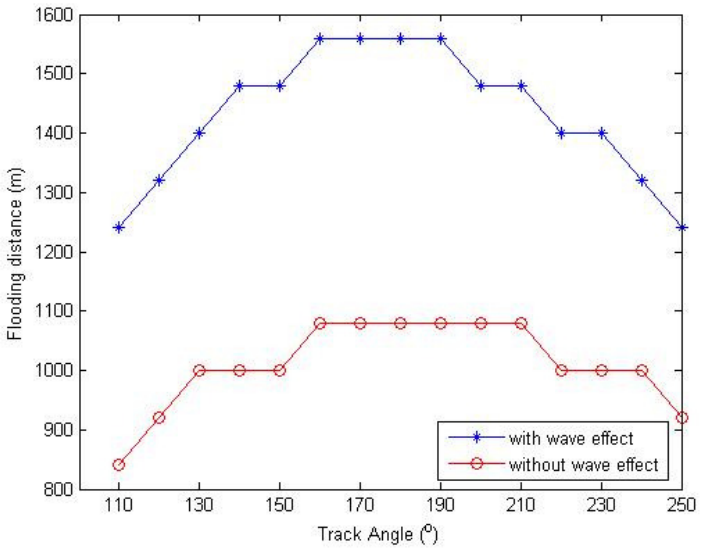

Figure 4.14: The effect of TC track on maximum inundation distance model with wave effect (blue line) and without wave effect (red line)

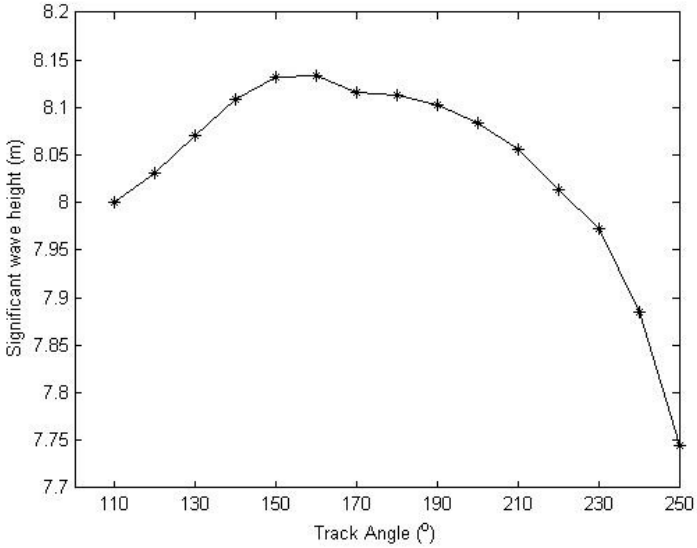

Figure 4.15: The effect of TC track on significant wave height using model with wave effect

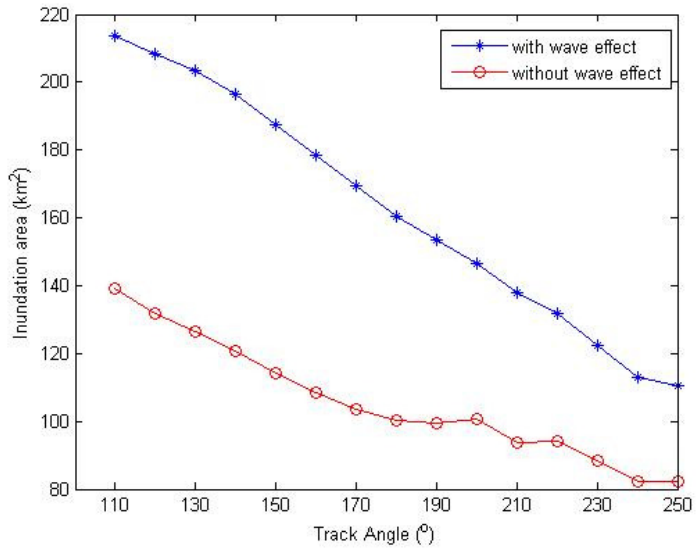

Figure 4.16: The effect of TC track on inundation area using model with wave effect (blue line) and without wave effect (red line)

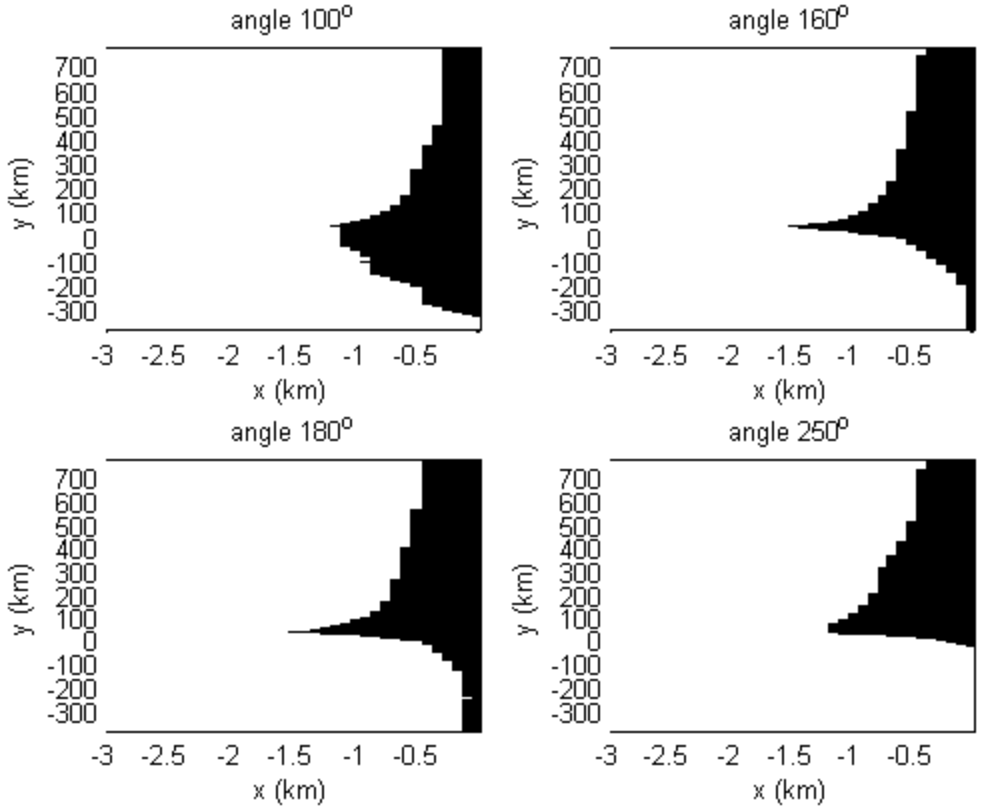

Figure 4.17: Total inundation area (black area) before TC landing with incident angles of 100^o (upper left panel), 160^o (upper right panel), 180^o (lower left panel) and 250^o (lower right panel), respectively, and with wave effect

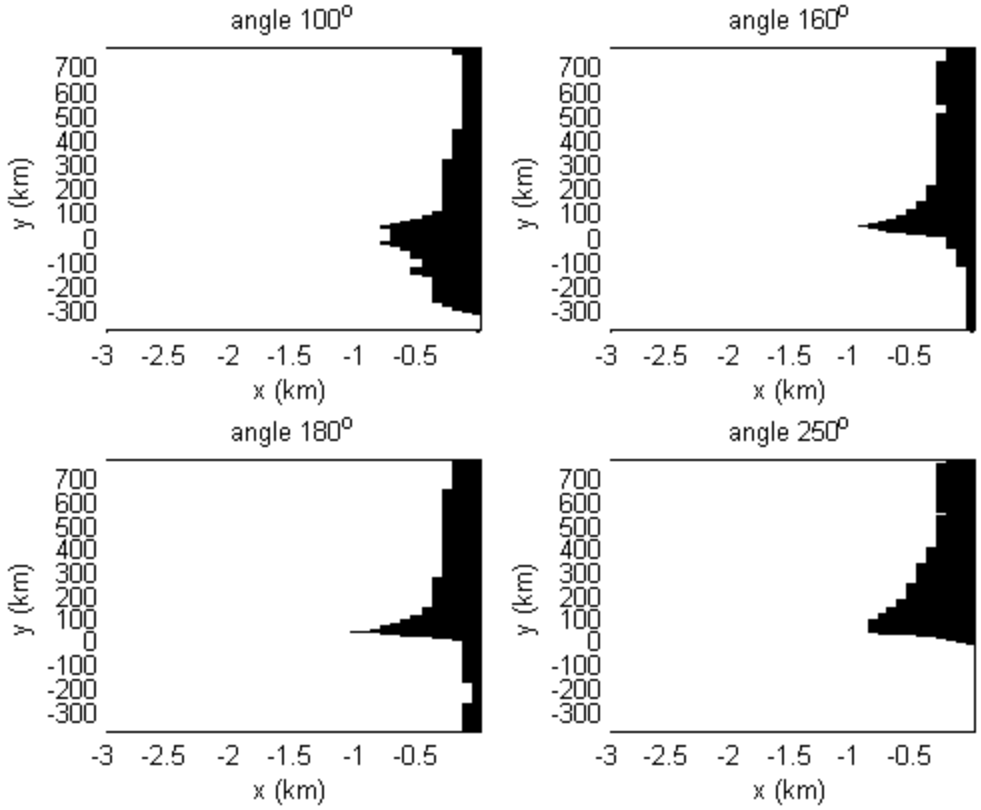

Figure 4.18: Total inundation area (black area) before TC landing with incident angles of 100^o (upper left panel), 160^o (upper right panel), 180^o (lower left panel) and 250^o (lower right panel), respectively, and without wave effect

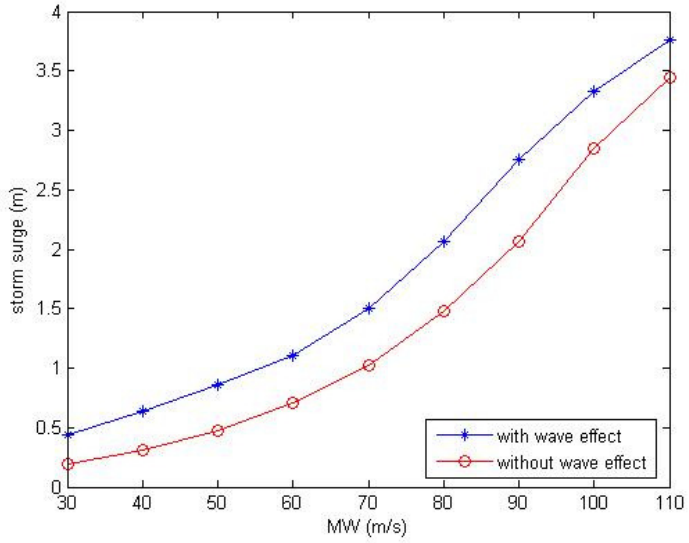

Figure 4.19: The effect of MW on peak storm surge using model with wave effect (blue line) and without wave effect (red line)

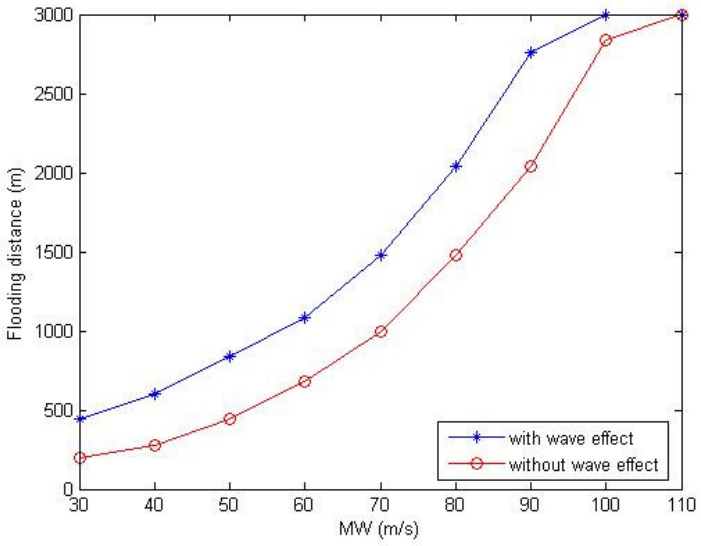

Figure 4.20: The effect of MW on maximum inundation distance using model with wave effect (blue line) and without wave effect (red line)

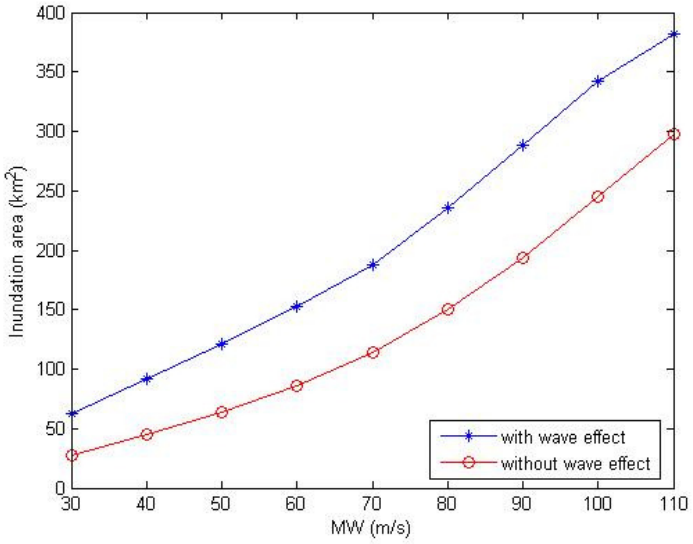

Figure 4.21: The effect of MW on inundation area using model with wave effect (blue line) and without wave effect (red line)

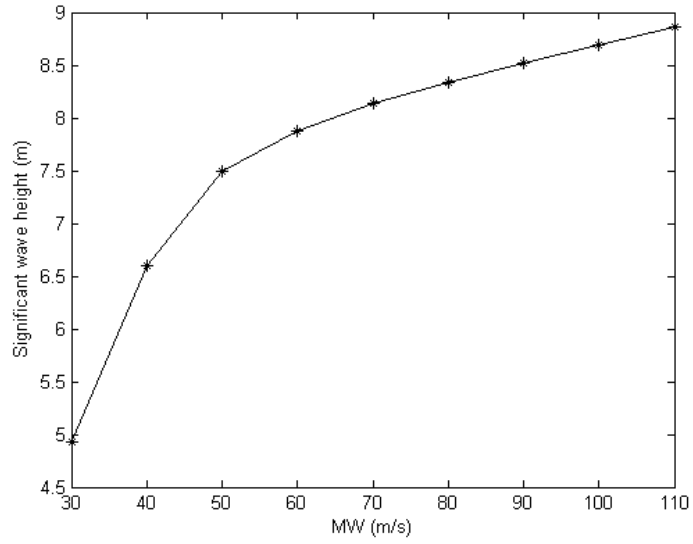

Figure 4.22: The effect of MW on significant wave height using model with wave effect

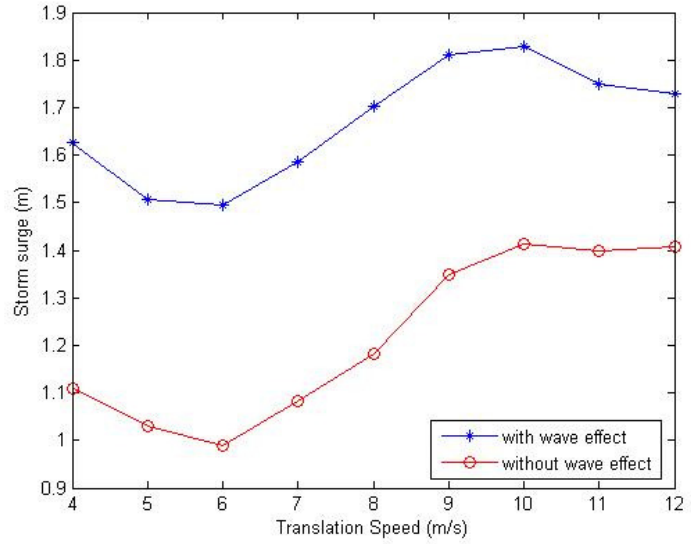

Figure 4.23: The effect of translation speed on peak storm surge using model with wave effect (blue line) and without wave effect (red line)

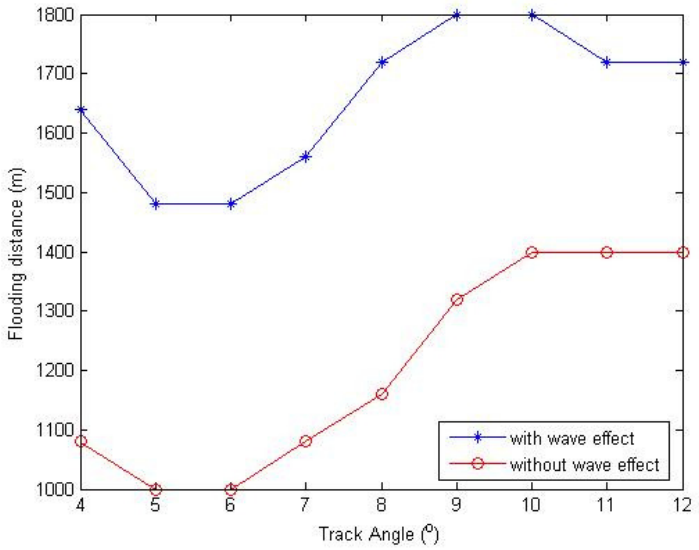

Figure 4.24: The effect of translation speed on maximum inundation distance using model with wave effect (blue line) and without wave effect (red line)

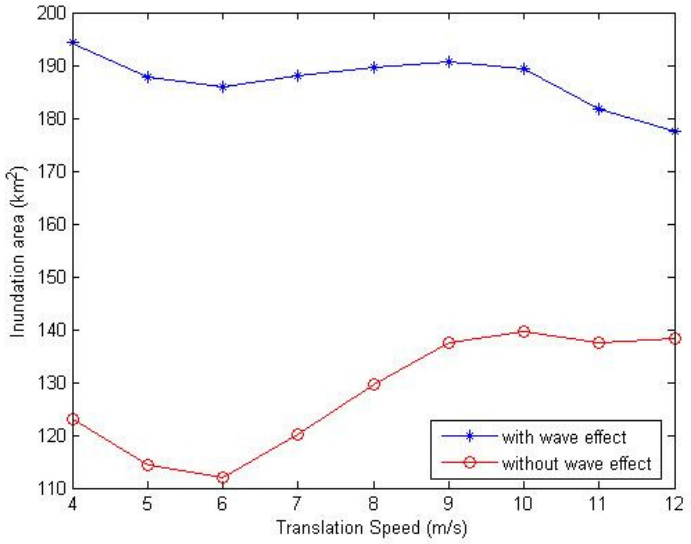

Figure 4.25: The effect of translation speed on inundation area using model with wave effect (blue line) and without wave effect (red line)

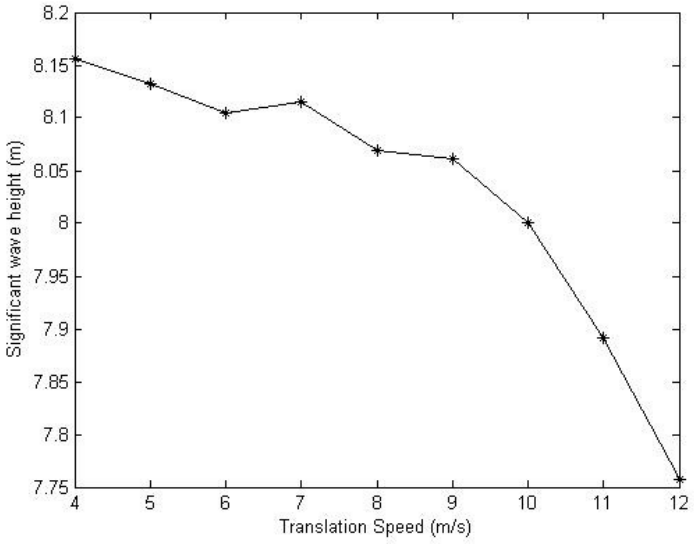

Figure 4.26: The effect of translation speed on significant wave height using model with wave effect

Chapter 5

CONCLUSION AND FUTURE WORK

5.1 Conclusion

The purpose of this study was to develop and test coupled wave-current systems for use in simulating and predicting storm-induced surges, waves and coastal inundation, and to explore the response of storm-induced waves, surges, and inundation to different cyclone parameters in conjunction with mechanism analysis through atmospheric forcing on ocean surface and wave forcing.

Two coupled systems were used in this study. They include an ocean circulation model (ROMS), an ocean wave model (SWAN) and a nearshore circulation model (SHORECIRC). Descriptions of the coupled system are presented including coupling framework as well as introductions of each model component and the couplers.

The coupled ROMS/SWAM system based on MCT implementation is applied to simulate currents and waves in Delaware Bay and the results are compared with available data set, such as ADCP current data set as well as wave data of May, 2005 from WSB, which was deployed to measure the surface at Fourteen Ft. Bank Lighthouse measuring station. The coupled model system is verified by comparisons between simulation result in Delaware Bay and observation data. The system performs well in

simulation of current velocity, wave height, wave energy as well as wave spectrum while the simulated peak frequency does not fit well the observations. Both experiment results and observation data show strong tidal modulations of surface waves, which indicate the importance of wave-current interaction during the numerical modeling.

The coupled SWAN/SHORECIRC system is based on the Master Program and is applied to a set of idealized experiments to investigate the sensitivity of storm-induced waves, surges, and inundations to different cyclone parameters. Four factors are taken into consideration for the sensitivity test: radius of maximum wind (RMW), the track of the TC, maximum wind speed (MW), and storm translation speed as well. In order to examine the effect of wave forcing on the coastal inundation, each experiment is carried out using models with and without wave effect in the system.

Storm-induced inundation is revealed to be sensitive to all of the four factors. Basically, the increase of RMW or the increase of MW will result in an increase of peak storm surge, significant wave height, and an increase of flooding area and flooding distance. The relationships are not linear. Inundation area is also very sensitive to the track of TC. When the track of TC changes from southeast to northeast (with an increase in incident angle), it generally predicts less severe inundation. However the storm surge is not changing monotonously with incident angles and the largest storm surge occurs at an incident angle of around 180^{o}. It also reveals the fact that the largest peak storm surge does not necessarily correspond to the largest inundated area. Storm surges and inundation are less sensitive to translation speed compared with other factors. One possible reason is that water pile-up vanishes in the idealized straight coast domain.

Wave forcing makes an important role in coastal inundation. Due to the effect of wave setup, model system with wave effect consistently produces larger storm surge, flooding distance and more severe inundation compared to the results without wave effect.

5.2 Suggestion for Future Work

Coupling between models with different scales, such as nearshore-scale circulation model and ocean-scale circulation model, has not been fully developed. It is suggested to develop a coupled system including both ocean-scale models and nearshore-scale models. Wind is believed to play an important role in the simulation and prediction of ocean circulations and waves. It is worthwhile to couple the meteorology model component into the coupled system.

BIBLIOGRAPHY

Arakawa, A. and Lamb, V. R., 1977, Methods of computational physics 17, 174-265, Academic Press

Battjes, J. A. and Janssen, J. P. F. M., 1978, "Energy loss and set-up due to breaking of random waves", Proc. 16th Int. Conf. Coastal Engineering, ASCE, 569-587

Bertotti, L. and Cavalieri, L., 1994, "Accuracy of wind and wave evaluation in coastal regions", Proc. 24 Int. Conf. Coastal Engineering, ASCE, 57-67

Bolonkin, A. A, 2006, "Cheap textile dam protection of seaport cities against hurricane storm surge waves, tsunamis, and other weather-related floods", http://arxiv.org

Booij, N., Ris, R. C., and Holthuijsen, L. H., 1999, "A third generation wave model for coastal regions 1. Model description and validation", J. Geophy. Res., 104, C4, 7649-7666

Carey, W. and Dalrymple, R. A., 2003, "Northeasters", Coastal Currents, Publications of University of Delaware Sea Grant College Program

Casulli V. and Zanolli, P., 2002, "Semi-implicit numerical modeling of nonhydro-static free-surface flows for environmental problems", Math. Comput. Model. 36, 1131-1149

Cavaleri, L. and Malanotte-Rizzoli, P., 1981, "Wind wave prediction shallow water: Theory and application", J. Geophys. Res., 86, C11, 10961-10973

Church, J. C., and Thornton, E. B., 1993, "Effects of breaking wave induced turbulence within a longshore current model", Coastal Eng., 20, 1-28

Dingemans, M. W., 1997, "Water wave propagation over uneven bottoms. Part 1 linear wave propagation", Advanced Series on Ocean Engineering, 13, World Scientific, 471 p

Egbert, G., Erofeeva, S., 2002, “Efficient inverse modeling of barotropic ocean tides”, Journal of Atmospheric and Oceanic Technology 19, 183-204

Eldeberky, Y. and Battjes, J.A., 1995, “Spectral modeling of wave breaking: Application to Boussinesq equations”, J. Geophys. Res., 102, 1253-1264

Freeman, N. G., Hale, A. M., and Danard, M. B., 1972, “A modified sigma equations; approach to the numerical modeling of great lake hydrodynamics”, J. Geophys. Res., 77(6), 1050-1060

Harper, B. A., Holland, G. J., 1999, “An updated parametric model of the tropical cyclone”, Proceedings of the 23rd Conference Hurricanes and Tropical Meteorology, 10-15 January 1999, American Meteorological Society, Dallas, TX

Hasselmann, S. and Hasselmann, K., 1981, “A symmetrical method of computing the non-linear transfer in a gravity-wave spectrum”, Hamburger Geophys. Einzelschr., Serie A., 52, 8

Hedstrom, K.S., 2000, “DRAFT Technical manual for a coupled Sea-Ice/Ocean Circulation Model (Version2)”, Institute of Marine and Coastal Sciences, Rutgers University

Holland, G. J., 1980, “An analytic model of the wind and pressure profiles in hurricanes”, Mon. Wea. Rev. 108, 1212-1218

Holthuijsen, L. H., Booij, N., Ris, R. C., Haagsma, IJ. G., Kieftenburg, A. T. M. M., Kriezi, E. E., Zijilema, M., Westhuysen, A. J. van der, 2004, “SWAN Cycle III version 40.31, User manual”, Department of Civil Engineering, Delft University of Technology, the Netherlands, February 5

Hsu, S. A., Yan, Z., 1998, “A note on the radius of maximum wind for hurricanes”, Journal of Coastal Research 14(2), 667-668

Jacob, R., Larson, J., Ong, E., 2005, “MxN communication and parallel interpolation in CCSM using the Model Coupling Toolkit”, Preprint ANL/MCSP1225-0205, Mathematics and Computer Science Division, Argonne National Laboratory, February 2005

Janssen, P. A. E. M., 1989, “Wave induced stree and the drag of air flow over sea waves”, J. Phys. Oceanogr, 19, 745-754

Janssen, P. A. E. M., 1991, “Quasi-linear theory of wind wave generation applied to wave forecasting”, J. Phys. Oceanogr, 21, 1631-1642

Johnson, H. K., 1999, “Simple expressions for correcting wind speed data for elevation”, Coastal Engineering, 36, 263-269

Kahman, K. K. and Calkoen, C. J., 1992, “Reconciling discrepancies in the observed growth of wind-generated waves”, J. Phys. Oceanogr., 22, 1389-1405

Komen, G. J., Hasselmann, S., and Hasselmann, K., 1984, “On the existence of a fully develop wind-sea spectrum”, J. Phys. Oceanogr., 14, 1271-1285

Larson, J., Jacob, R., Ong, E., 2004, “The Model Coupling Toolkit: A new Fortran90 toolkit for building multiphysics parallel coupled models”, Preprint ANL/MCSP1208-1204, Mathematics and Computer Science Division, Argonne National Laboratory, December 2004

Li, M., Zhong, L., Boicourt, W. C., Zhang, S. and Zhang, D., 2006, “Hurricane-induced storm surges, currents and destratification in a semi-enclosed bay”, Geophy. Res. Letter, 33, L02604

Liu, H., and Xie, L., 2009, “A numerical study on the effects of wave-current-surge interactions on the height and propagation of sea surface waves in Charleston Harbor during Hurricane Hugo 1989”, Continental Shelf Res., 29, 11-15, 1454-1463

Longuet-Higgins, M. S., and Stewart, R. W., 1962, “Radiation stress and mass transport in gravity waves, with application to ‘surf beats’”, J. Fluid Mech, 13, 481-504

Longuet-Higgins, M. S., and Stewart, R. W., 1964, “Radiation stress in water waves, a physical discussion with application”, Deep Sea Res, 11, 529-563

Madsen, O.S., Poon, Y. K., and Graber, H. C., 1988, “Spectral wave attenuation by bottom friction: Theory”, Proc. 21th Int. Conf. Coastal Engineering, ASCE, 492-504

Mellor, F., 2008, “The depth-dependent current and wave interaction equation: A revision”, J. Phys. Oceanogr, 38(11), 2587

Miles, J.W., 1957, “On the generation of surface waves by shear flows”, J. Fluid Mech., 3, 185-204

Padilla-Hernandez R., Perrie, W., Toulany, B., Smith, P. C., Zhang, W., and Jimenez-Hernandez, S., 2004, "Intercomparison of modern operational wave models", 8th International Workshop on Wave Hindcasting and Forecasting, North Shore, Oahu, Hawaii, November 2004

Peng, M., Xie, L., Pietrafesa, L., 2004, "A numerical study of storm surge and inundation in the Croatan-Albemarle-Pamlico Estuary System", Estuarine, Coastal and Shelf Science 59, 121-137

Peng, M., Xie, L., Pietrafesa, L., 2006, "Tropical cyclone induced asymmetry of sea level surge and fall and its presentation in a storm surge model with parametric wind fields", Ocean Modelling 14, 81-101

Penven, P. and Tan, T. J., 2007, "ROMSTOOLS user's guide", Institute de Recherche pour le Development, Paris, France

Phillips, N. A., 1957, "A coordinate system having some special advantages for numerical forecasting", J. Meteorology, 14(2), 184-185

Pierson, W.J. and Moskowitz, L., 1964, "A proposed spectral form for fully developed wind seas based on the similarity theory of S.A. Kitaigorodskii", J. Geophys. Res., 69, 24, 5181-5190

Qin, W., 2005, "Application of the spectral wave model SWAN in Delaware Bay", Master Thesis, University of Delaware

Ris R. C., Holthuijsen, L. H., and Booij, N., 1999, "A third generation wave model for coastal regions 2. Verification", J. Geophy. Res., 104, C4, 7667-7681

Shchepetkin, A. F. and McWilliams, J. C., 2005, "The regional ocean modeling system: A split-explicit, free-surface, topography-following coordinates ocean model", Ocean Model., 9, 347-404

Shemdin, P., Hasselmann, K., Hsiao, S. V., and Herterich, K., 1978, "Non-linear and linear bottom interaction effects in shallow water, in: Turbulent Fluxes through the Sea Surface, Wave Dynamics and Prediction", NATO Conf. Ser., V, 1, 347-372

Shi, F., Hanes, D. M., Kirby, J. T., Erikson, L., Barnard, P., and Eshleman, J., 2009, "Pressure gradient-dominated nearshore circulation on a beach influenced by an adjacent large inlet", J. Geophy. Res., in revision

Shi F., Kirby, J. T., and Hanes D. M., 2007, "An efficient mode-splitting method for a curvilinear nearshore circulation model", Coastal Engineering, 54, 811 – 824

Shi, F., Kirby, J. T., Newberger, P. A., and Haas, K., 2005, "NearCoM master program, version 2005.4, User's manual and module integration", CACR 2005-3, Center for Applied Coastal Research, University of Delaware, Newark

Shi F., Svendsen, I. A, Kirby, J. T., and Smith, J. M., 2003, "A curvilinear version of a Quasi-3D nearshore circulation model", Coastal Engineering, 49, 99-124

Smith, M. H., Park, P. M., and Consterdine, I. E., 1993, "Marine aerosol concentrations and estimated fluxes over the sea", Q.J.R. Meteorol. Soc., 119, 809-824

Song, Y. and Haidvogel, D. B., 1994, "A semi-implicit ocean circulation model using a generalized topography-following coordinate system", J. Comp. Phys., 115(1), 228-244

Styles, R. and Glenn, S. M., 2000, "Modeling stratified combined wave-current bottom boundary layers", J. Geophysical Research, 101, 24119-24139

Svendsen, I. A., Hass, K., and Zhao, Q., 2000, "Quasi-3D nearshore circulation model, SHORECIRC, Version 1.3.6", Report, Center for Applied Coastal Research, University of Delaware, Newark

Vickery, P. J., Skerlj, P. F., Steckley, A. C., Twisdale, L. A., 2000, "Hurricane wind field model for use in hurricane simulations", J. Strut. Eng., 1203-1221

WAMDI Group, 1988, "The WAM model - a third generation ocean wave prediction model", J. Phys. Oceanogr., 18, 1775-1810

Warner, J. C., Sherwood, C. R., Signell, R. P., Harris, C. K. and Arango, H. G., 2008, "Development of a three-dimensional, regional, coupled wave, current, and sediment-transport model", Computers and Geosciences, 34, 10, 1284-1306

Weisberg, R. H. and Zheng, L, 2008, “Hurricane storm surge simulations comparing three-dimensional with two-dimensional formulations based on an Ivan-like storm over the Tampa Bay, Florida region”, Journal of geophysical research. C, Oceans, 113, C12

Whitham, G. B., 1974, “Linear and nonlinear waves”, Wiley, New York, 636 p.

Whitney, M. M., 2003, “Simulating the Delaware coastal current”, Ph.D. Dissertation, University of Delaware, DE, USA

Wilkin, J. and Hedstrom, K. S., 1991, “User's manual for an orthogonal curvilinear grid-generation package”, Institute for Naval Oceanography

Zhang, M. Y. and Li, Y. S., 1997, “The dynamic coupling of a 3rd-generation wave model and a 3d hydrodynamic model through boundary-layers”, Cont. Shelf Res. 17 (1997), pp. 1141–1170